JGR Solid Earth

Key Points:
- We propose a statistical seismicity model that explicitly incorporates the seismicity-triggering effects of slow slip events (SSEs)
- Our model assumes a linear or power relationship between SSE moment rates and seismicity rates and estimates its proportional constant
- We applied our model to SSEs in the Hikurangi Trench, New Zealand, and evaluated its performance

Author Contributions:
Investigation: Tomoaki Nishikawa
Methodology: Tomoaki Nishikawa
Supervision: Takuya Nishimura
Validation: Takuya Nishimura
Visualization: Tomoaki Nishikawa
Writing – original draft: Tomoaki Nishikawa
Writing – review & editing: Takuya Nishimura

Development of an Epidemic-Type Aftershock-Sequence Model Explicitly Incorporating the Seismicity-Triggering Effects of Slow Slip Events

Tomoaki Nishikawa[1] and **Takuya Nishimura**[1]

[1]Disaster Prevention Research Institute, Kyoto University, Kyoto, Japan

Abstract Slow slip events (SSEs) at subduction zone plate boundaries sometimes trigger earthquake swarms and megathrust earthquakes. The causal relationship between SSEs and seismicity has been studied worldwide, but the epidemic-type aftershock-sequence (ETAS) model, which is a standard statistical model of seismicity, does not explicitly consider the seismicity-triggering effect of SSEs. Therefore, if an SSE occurs at a plate boundary, probabilistic earthquake forecasts based on the ETAS model fail to predict observed seismicity. Here, we constructed a statistical model named the SSE-modulated ETAS model by incorporating SSE moment rates estimated from observation data from the global navigation satellite system into the original ETAS model. Our model assumes a linear or power-law relationship between the SSE moment rates and seismicity rates and estimates its proportionality constant as a new ETAS parameter. We applied this new model to three SSEs and M 2.5 or greater earthquakes in the shallow part of the Hikurangi Trench, New Zealand. The results show that it is better than the original ETAS model, giving a significant reduction in the Akaike information criterion. In addition, we examined the functional forms (e.g., lag time and power exponent) of the equation relating the moment rate of the SSEs to the seismicity rate. We also examine the influence of SSEs on aftershock productivity. Our model can improve short-term forecasts of seismicity associated with SSEs if the detection and characterization of SSEs can be done in near real time. Our model is also useful for quantifying characteristics of SSE-induced seismicity.

Plain Language Summary Slow slip events (SSEs) are episodic slow fault-slip phenomena. They frequently occur at tectonic plate boundaries and sometimes induce large earthquakes and swarms of small-to-moderate earthquakes. The relationship between SSEs and seismicity has been actively studied. However, the epidemic-type aftershock-sequence (ETAS) model, which is a statistical seismicity model widely used to forecast earthquakes, does not consider the effects of SSEs inducing earthquakes. Therefore, this model cannot predict seismicity associated with SSEs. In this study, we made a new ETAS model by incorporating SSE source properties estimated from geodetic data into the original ETAS model. We applied this new model to SSEs and earthquakes observed in the shallow part of the Hikurangi subduction zone, which is a subduction plate boundary off New Zealand's North Island. We found that the predictions of the new model are significantly better than those of the original ETAS model. Our new model is useful for forecasting and investigating seismicity induced by SSEs.

1. Introduction

Slow slip events (SSEs) are episodic slow fault-slip phenomena. SSEs at subduction plate boundaries sometimes trigger earthquake swarms, which are seismic sequences without distinguishable mainshocks, in their vicinities. Earthquake swarm activities synchronized with SSEs have been observed in many circum-Pacific subduction zones, including the Japan Trench (Ito et al., 2013; Kawasaki et al., 1995; Nishikawa et al., 2023), Nankai Trough (Yamamoto et al., 2022), Sagami Trough (Ozawa et al., 2003), Hikurangi Trench of New Zealand (Delahaye et al., 2009; Nishikawa et al., 2021; Wallace et al., 2012), and the subduction zones of Ecuador (Collot et al., 2017; Vallée et al., 2013), Peru (Villegas-Lanza et al., 2016), Mexico (Liu et al., 2007; Nishikawa & Ide, 2017), and northern Chile (Socquet et al., 2017). SSEs can trigger not only earthquake swarms, but also megathrust earthquakes. Such examples have recently been reported for the Mexican subduction zone (Cruz-Atienza et al., 2021; Radiguet et al., 2016). In light of these observations, it is important to evaluate the extent to which SSEs increase the seismicity rate and probability of earthquake occurrence to improve short-term seismic hazard assessments.

Statistical seismicity models are useful for estimating the probability of earthquake occurrence. The epidemic-type aftershock-sequence (ETAS) model (Ogata, 1988) is a standard statistical model of seismicity. This model expresses the seismicity rate as the summation of the stationary background seismicity rate and aftershock rates derived from Omori–Utsu's aftershock law (e.g., Utsu, 1957; Utsu et al., 1995). The ETAS model successfully describes the earthquake-to-earthquake triggering effect and is widely used to calculate the probability of earthquake occurrence (e.g., Schorlemmer et al., 2018). However, a problem with this model is that it cannot describe well seismicity associated with transient aseismic phenomena (e.g., SSEs and crustal fluid migration). For example, many previous studies have shown that the occurrence of an SSE at a plate boundary causes a large discrepancy between observed seismicity and prediction by the ETAS model; that is, many more earthquakes are observed than predicted by the ETAS model (e.g., Llenos et al., 2009; Nishikawa & Ide, 2018; Okutani & Ide, 2011; Reverso et al., 2016). We note that several studies utilized this defect of the ETAS model to detect possible aseismic transients (e.g., Marsan et al., 2013; Nishikawa & Ide, 2017; Okutani & Ide, 2011).

To resolve the problem with the original ETAS model, Llenos et al. (2009) proposed adding a term that represents SSE-induced seismicity to the original ETAS model (e.g., Ogata, 1988; Zhuang et al., 2002). Following this concept, Llenos and McGuire (2011) considered the difference between the seismicity rate predicted by the conventional ETAS model and the observed seismicity rate to be the increase in the background seismicity rate due to SSEs. Furthermore, Okutani and Ide (2011) expressed an SSE-induced increase in the seismicity rate within the framework of the conventional ETAS model by assigning different sets of ETAS parameters to SSE and non-SSE periods. Moreover, we note that Llenos and Michael (2019) proposed a sophisticated version of the ETAS model to predict seismicity rate increases associated with complex fluid and fault interaction processes, which may also be applicable to SSE-induced seismicity. However, these models do not explicitly consider the geodetically estimated source properties of the SSEs. Therefore, important equations, such as the equation relating the SSE moment rate to the seismicity rate of SSE-induced earthquakes, were not formulated in these models. In other words, these models cannot answer the question "How many earthquakes are expected to be triggered when an SSE of a certain size occurs?" within their framework.

In contrast to Llenos et al. (2009) and Okutani and Ide (2011), who used the temporal ETAS model (Ogata, 1988), Reverso et al. (2016) performed an analysis similar to Okutani and Ide (2011) using the spatiotemporal ETAS model (Ogata, 2011; Zhuang et al., 2002). The spatiotemporal ETAS model considers not only the origin times of earthquakes but also their epicentral locations. Reverso et al. (2016) assigned different ETAS parameters to SSE and non-SSE periods for five SSEs in the Sagami Trough, eastern Japan. They compared the estimated ETAS parameters and the seismic moments of these SSEs and obtained an equation relating the SSE seismic moment to the number of SSE-induced earthquakes. However, their equation has not been used to improve the original ETAS model. Regardless of whether it is a temporal model or spatiotemporal model, no ETAS model that explicitly incorporates geodetically estimated SSE source properties has been created. Furthermore, the analysis of Reverso et al. (2016) was based on somewhat simplistic assumptions: they fixed the durations of SSE-induced seismicity to 10 days and assumed that the background seismicity rate during the SSE period was constant, regardless of various temporal evolutions of SSEs estimated from the geodetic data (e.g., Fukuda, 2018).

In addition to the ETAS model, the rate- and state-dependent friction (RSF) seismicity model (Dieterich, 1994) is known as a standard seismicity model. This model is based on a friction law derived from rock friction experiments (Dieterich, 1979), in contrast to the ETAS model, which is purely empirical. Because it relates the stressing rate on a fault to the seismicity rate, this model can predict the seismicity rate change associated with a stress transient, regardless of whether the cause of the stress transient was seismic or aseismic (Segall et al., 2006). However, we note that Llenos et al. (2009) pointed out a discrepancy between the model and an observed fact: it failed to predict the number of aftershocks of a M 5.1 earthquake triggered by the 2005 Salton Trough SSE, with the predicted number being hundreds of times larger than what was observed. They suggested that the discrepancy was due to a feature of the RSF seismicity model that not only the background seismicity rate but also the aftershock rate immediately following the mainshock is approximately proportional to the stressing rate on a fault.

In light of the above studies, this study aims to develop the first ETAS model that explicitly incorporates geodetically estimated SSE source properties to describe the triggering effect of SSEs on seismicity. We regard this study as a first step in improving the existing ETAS models. Therefore, we worked on improving the simplest ETAS model, that is, the temporal ETAS model (Ogata, 1988), rather than the spatiotemporal ETAS model (Ogata, 2011; Reverso et al., 2016; Zhuang et al., 2002). This study is a direct improvement of the temporal ETAS
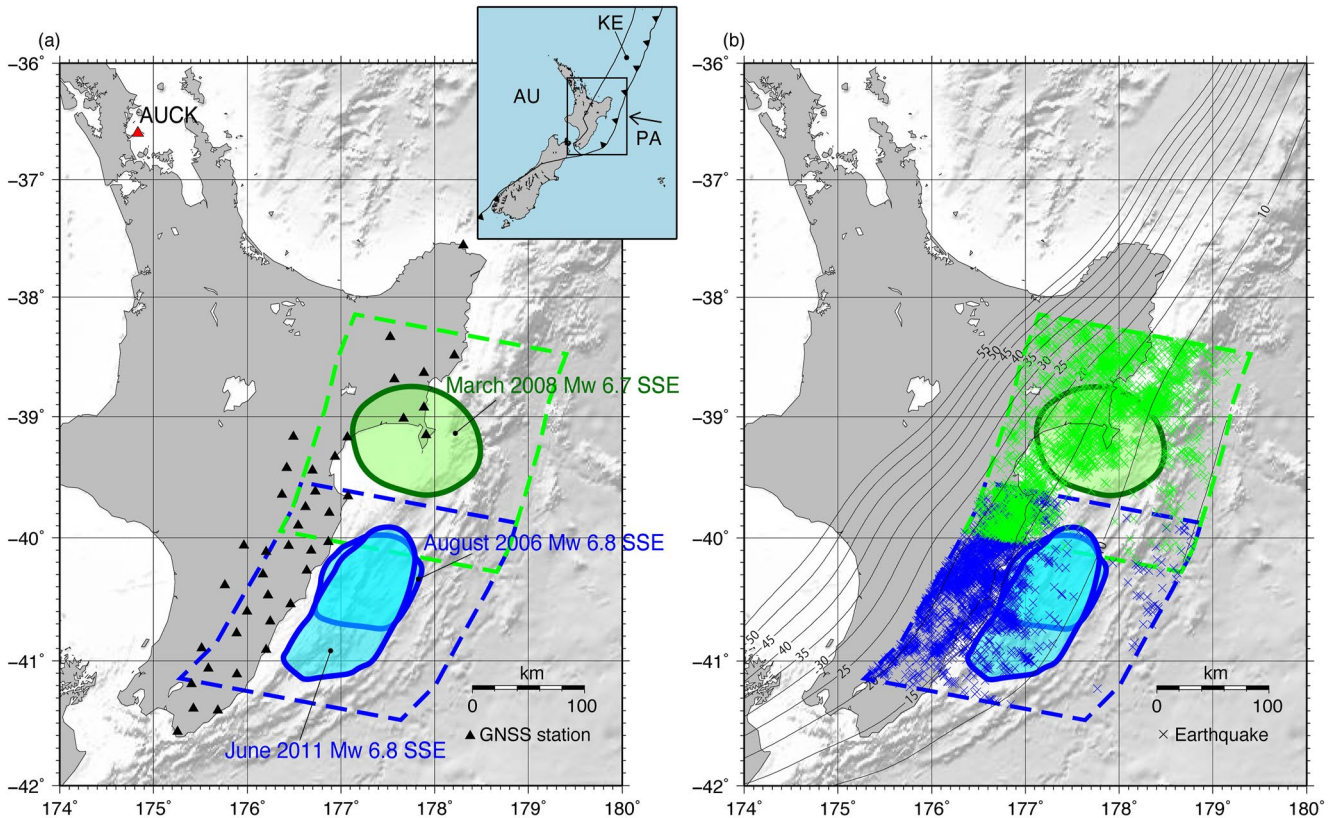
Figure 1. Analyzed slow slip events (SSEs) and seismicity (a) Distribution of the analyzed SSEs and global navigation satellite system (GNSS) stations used in this study. The two overlapped blue-shaded areas indicate the source regions of the August 2006 M_w 6.8 and June 2011 M_w 6.8 SSEs that occurred in the south-central part of the Hikurangi Trench. The green-shaded area is the source region of the March 2008 M_w 6.7 SSE, which occurred in the north-central part of the Hikurangi Trench. The source regions are based on the results of this study (see Sections 3.1.1, 3.2.1, and 3.3.1) (15 mm or larger slip). The locations and spatial scales of the source regions generally agree with those obtained in the previous studies (Wallace & Beavan, 2010; Wallace et al., 2012). The dashed blue polygon is the study region used for the epidemic-type aftershock-sequence (ETAS) analyses of the 2006 and 2011 SSEs and their nearby seismicity. The dashed green polygon denotes the study region used for the ETAS analysis of the 2008 SSE and its nearby seismicity. The black triangles indicate GNSS stations used to estimate the moment rates of the SSEs. The red triangle denotes station AUCK, which we fixed to calculate the GNSS displacements. The inset map shows the tectonic setting of the Hikurangi Trench, where PA, KE, and AU denote the Pacific, Kermadec, and Australian plates, respectively (Bird, 2003). The black arrow represents the PA plate motion relative to KE. (b) Distribution of the analyzed seismicity. Small blue crosses are epicenters of M 2.5 or greater earthquakes within the dashed blue polygon from 2006 to 2011. Green small crosses are epicenters of M 2.5 or greater earthquakes within the dashed green polygon from 2006 to 2008. The earthquakes are from the GeoNet earthquake catalog. Black contours are depth contours of the plate interface (5-km interval; Hayes, 2018). ETAS, epidemic-type aftershock-sequence; SSE, slow slip event.

models of Llenos et al. (2009) and Okutani and Ide (2011). Our model assumes a linear or power-law relationship between the SSE moment rate and the SSE-induced seismicity rate, and estimates its proportionality constant as a new ETAS parameter. This model enabled us to better estimate the probability of earthquake occurrence by considering increases in the seismicity rate due to SSEs. Furthermore, from this model, we successfully obtain a formulation of seismicity that includes an equation relating SSE moment rates to SSE-induced seismicity rates.

To examine the performance of our new model, we applied it to SSEs in the shallow part of the Hikurangi Trench and nearby seismicity (Figure 1). In the Hikurangi Trench, the Pacific Plate subducts under the Kermadec Plate (Bird, 2003), causing the frequent occurrence of short-term (one month or shorter) SSEs on the shallow plate interface (20 km or shallower) (e.g., Wallace, 2020; Wallace & Beavan, 2010; Wallace et al., 2012). These shallow SSEs are often accompanied by earthquake swarms (e.g., Delahaye et al., 2009). Furthermore, the Hikurangi Trench is an intriguing subduction zone where various temporal relationships between SSEs and earthquake swarms have been reported (Nishikawa et al., 2021; Shaddox & Schwartz, 2019; Todd et al., 2018). Sometimes, an SSE and earthquake swarm coincide, and at other times, a clear time lag is observed between them. Moreover, some SSEs occur without triggering detectable earthquake swarms (Nishikawa et al., 2021). By applying our new model, we aimed to quantify the relationships between SSEs and seismicity in the Hikurangi Trench and gain insights into the physical mechanisms of SSE-induced seismicity.

2. Data and Methods

2.1. Analyzed SSEs and Study Regions

We focused our analysis on three SSEs at the shallow plate boundary of the Hikurangi Trench (Figure 1). The three SSEs occurred in the central part of the Hikurangi Trench (39°S to 41°S), with two (M_w 6.8 in August 2006 and M_w 6.8 in June 2011) located in the south-central part (Wallace & Beavan, 2010; Wallace et al., 2012) and one (M_w 6.7 in March 2008) in the north-central part (Wallace & Beavan, 2010). According to the previous studies (Wallace & Beavan, 2010; Wallace et al., 2012), the duration of the 2006, 2011, and 2008 SSEs was 7 days, 32 days, and 15 days, respectively. It should be noted, however, that the SSE durations in the previous studies were determined by visual inspection of global navigation satellite system (GNSS) time-series data and are subject to large uncertainties. The three analyzed SSEs are relatively large (M_w 6.7 to 6.8) compared to other SSEs in the shallow part of the Hikurangi Trench (M_w 5.6 to 6.9) (Nishikawa et al., 2021; Wallace & Beavan, 2010; Wallace et al., 2012). We selected these SSEs for analysis because of their clear geodetic signals and their isolation in time. We were interested in the seismicity-triggering effects of individual large SSEs and their variations (see the discussion in Section 4.1) and preferred relatively simple slip events for our analysis. Therefore, we did not select complex slip events such as the January and March 2010 SSEs in the north-central part of the Hikurangi Trench (Wallace & Beavan, 2010; Section 4.6), in which two large SSEs ($M_w \geq 6.7$) occurred a short time interval apart (about one month), for our analysis.

We used two partially overlapping study regions for our ETAS model analyses (Figure 1). Both study regions were approximately 200-km long in the directions of the strike and plate motion. We used the SSE slip inversion results from previous studies (Wallace & Beavan, 2010; Wallace et al., 2012) and this study (see Sections 3.1.1, 3.2.1, and 3.3.1) and the epicenters of known earthquake swarms accompanying these SSEs (Nishikawa et al., 2021; Wallace et al., 2012) as references to choose the study regions. The study regions enclose the SSE slips and the epicenters of the earthquake swarms. We used the same study region (the blue dashed polygon in Figure 1a) for the 2006 and 2011 SSEs because of the substantial overlap in their source areas. Hereafter, we refer to the study region colored blue as the southern study region and that colored green as the northern study region. We discuss the influence of the size of the study regions on our results in Text S1 in Supporting Information S1.

2.2. Earthquake Catalog and Global Navigation Satellite System Data

We analyzed the seismicity during 3-year periods that included the occurrence period of each SSE. For the 2006 and 2008 SSEs in the south-central and north-central parts of the Hikurangi Trench, we used the period from January 2006 to December 2008. For the 2011 SSE in the south-central part, we used the period from January 2009 to December 2011. If we use a longer period (e.g., 6 years or longer), the time window will include multiple large SSEs ($M_w \geq 6.7$). In this study, we chose the relatively short periods of 3 years because we were interested in quantifying the seismicity-triggering effects of individual large SSEs (see the discussion in Section 4.1), rather than the seismicity-triggering effects averaged over multiple large SSEs. We discuss the influence of the length of the study periods on our results in Text S1 in Supporting Information S1.

We extracted earthquakes that occurred in the study regions during the analysis period from the GeoNet earthquake catalog (Figure 1b). GeoNet (https://www.geonet.org.nz) routinely archives earthquakes around New Zealand. We extracted the earthquakes regardless of their source depths, because previous studies have shown that not only interplate seismicity but also intraslab and upper-plate seismicity are associated with SSEs on the plate interface of the Hikurangi Trench (Hughes et al., 2021; Jacobs et al., 2016; Nishikawa et al., 2021; Shaddox & Schwartz, 2019; Warren-Smith et al., 2019; Yarce et al., 2019).

We then estimated the magnitude of completeness for each region and period using the MAXC method, with a correction value of 0.2 (Wiemer & Wyss, 2000; Woessner & Wiemer, 2005). We showed the earthquake size-frequency distributions of the analyzed earthquakes in Figure S1 in Supporting Information S1. In the southern study region (the dashed blue polygon in Figure 1a), we found that the magnitude completeness values are 2.5 and 2.4 for the 2006–2008 and 2009–2011 analysis periods, respectively. In the northern study region (the dashed green polygon in Figure 1a), the magnitude completeness value is 2.6 for the 2006–2008 period. When comparing the analysis results, it is desirable to use the same minimum magnitude for all the study regions and analysis periods. Therefore, we set the minimum magnitude to M 2.5 for all study regions and periods. For the 2008 SSE in the northern study region, the minimum magnitude (M 2.5) was smaller than the magnitude completeness value

(M 2.6). Therefore, for the 2008 SSE, we repeated our analyses using M 2.6 or greater earthquakes and confirmed that the slight incompleteness of the catalog did not affect our conclusions.

The GeoNet earthquake catalog changed its earthquake location algorithm in 2012, and its earthquake location procedure was fully automated. This worsened the quality of the catalog from January 2012; the magnitude completeness value has been reported to be larger than M 3.0 from January 2012 (Nishikawa et al., 2021). Because of the incompleteness of the earthquake catalog, we did not analyze SSEs and seismicity after January 2012.

If a large earthquake occurs just outside the boundaries of the study regions, its aftershock activity could occur inside the study regions and affect the estimation of ETAS parameters. To address this concern, we inspected seismicity that occurred just outside the boundaries. As a result, we found that no large earthquakes (M 5 or greater) with aftershock activity (M 2.5 or larger) within the study regions had occurred during the analysis period (January 2006 to December 2011). Therefore, the seismicity just outside the boundaries of the study regions is unlikely to have a significant impact on the estimation of ETAS parameters.

To estimate the moment rates of the SSEs, we used time-series data from a continuous global navigation satellite system (GNSS) observation network operated by GeoNet. We used three components (i.e., east–west, north–south, and up–down). The daily time-series solutions are available at https://www.geonet.org.nz/data/types/geodetic. For details on the analysis strategy for the solutions, see the website.

We estimated the moment rates of the 2006 and 2011 SSEs using coastal GNSS stations south of 39.1°S (19 and 30 stations, respectively) and that of the 2008 SSE using coastal stations north of 39.8°S (13 stations) (see Figure 1a). We selected coastal stations that were in operation during the SSE periods. We used daily coordinates within 120-day time windows, whose centers correspond with the central date of each SSE period. The central date of each SSE period (31 August 2006; 29 June 2011; and 25 March 2008) was based on Wallace and Beavan (2010) and Wallace et al. (2012). We fixed station AUCK (the red triangle in Figure 1) to calculate the GNSS displacements. We visually inspected the time-series data of each GNSS station and did not use stations anomalously noisy or significantly affected by transient displacements other than those caused by the three analyzed SSEs. We confirmed that no major earthquake (M_w 6 or greater) that could cause a large coseismic displacement had occurred during the time windows, and that there was no artificial offset due to GNSS equipment changes.

2.3. SSE-Modulated ETAS Model

2.3.1. Model Formulation

The ETAS model (Ogata, 1988) expresses the seismicity rate as the summation of the stationary background seismicity rate and aftershock rates derived from Omori–Utsu's aftershock law:

$$\lambda(t) = \mu + \sum_{t_i < t} \frac{K e^{\alpha(M_i - M_c)}}{(t - t_i + c)^p} \tag{1}$$

where $\lambda(t)$ is the seismicity rate at time t, μ is the stationary background seismicity rate, and the second term on the right-hand side is the summation of aftershock rates of earthquakes of magnitude M_i and origin time t_i ($<t$). The aftershock rates are assumed to show power-law decay (Omori-Utsu's aftershock law; Utsu, 1957; Utsu et al., 1995). They are controlled by four ETAS parameters: α, c, K, and p. M_c is the minimum magnitude of the earthquake catalog, which we fixed to M 2.5 (see Section 2.2). In the following analyses, the units of the parameters are as follows: μ (events/day), c (days), and K (events/day^ $(1 - p)$). α and p are dimensionless. The unit of K (events/day^ $(1 - p)$) is tricky because it depends on the p-value. Strictly speaking, we cannot directly compare K-values when p-values are different. Instead, we can indirectly compare them by integrating the aftershock rate for a given time interval or computing the aftershock rate at a given time.

The original ETAS model (Equation 1) cannot describe well seismicity triggered by SSEs because it does not include a time-varying term associated with the occurrence of SSEs. Llenos et al. (2009) analyzed the seismicity associated with the 2005 Salton Trough SSE in California, the 2005 Kilauea SSE in Hawaii, and the 2002 and 2007 Boso-Oki SSEs in the Sagami Trough using the original ETAS model. They found that these SSEs had substantially increased the background seismicity rate (μ) by one to four orders of magnitude. In contrast, they found that the aftershock productivity (K) had changed only by factors of 0.5–3. Their results suggest that SSEs predominantly increase the background seismicity rate without substantially changing aftershock rates. Based on

the findings of Llenos et al. (2009), we mainly consider the influence of SSEs on the background seismicity rate in the subsequent analyses (Section 3), although we discuss the influence of SSEs on aftershock productivity in Section 4.3.

We formulated our new model as follows:

$$\lambda(t) = \mu + A(t) + \sum_{t_i < t} \frac{K(t)e^{\alpha(M_i - M_c)}}{(t - t_i + c)^p},\tag{2}$$

where $A(t)$ represents an increase in the background seismicity rate due to an SSE and $K(t)$ represents the change in the aftershock productivity due to the SSE. In subsequent analyses, except in Section 4.3, we assume that $K(t)$ is stationary ($K(t) = K$). That is, SSEs do not affect aftershock productivity.

Here, we assume the following function form for $A(t)$:

$$A(t) = \eta \left\{ \dot{M}_0^{\mathrm{SSE}}(t - \tau) \right\}^\gamma \tag{3}$$

where $\dot{M}_0^{\mathrm{SSE}}(t)$ is the moment rate of the SSE, η is the proportionality constant between the SSE moment rate and the rate of earthquakes triggered by the SSE, γ is the power exponent between the SSE moment rate and seismicity rate, and τ is the lag time between the SSE moment rate and seismicity rate. We assumed a power-law relationship between the SSE moment rate and seismicity rate based on observations of five SSEs in the Sagami Trough that showed clear correlations between SSE moment rates and seismicity rates (Fukuda, 2018; Reverso et al., 2016). Although more complex functional forms are possible, the power-law relationship seems simple and reasonable given that the previous observation (Reverso et al., 2016) implied a linear relationship. We introduced the parameter describing lag time, considering previous studies reporting lag times of a few days to a month between SSEs and associated seismicity in the Hikurangi Trench (Nishikawa et al., 2021; Shaddox & Schwartz, 2019; Todd et al., 2018). If $\tau = 0$, the seismicity rate increases concurrently with SSE. We assumed τ to be non-negative because of our implicit assumption of causality between SSEs and associated seismicity. However, Nishikawa et al. (2021) reported that seismicity rate increases sometimes preceded SSEs in the Hikurangi Trench. We leave modeling such seismicity, whose causal relationship with SSEs is unclear, for future work. For simplicity, in the following analyses, except in Sections 3.1.3, 3.2.3, and 3.3.3, we assume $\tau = 0$ (no lag time) and $\gamma = 1$ (a linear relationship):

$$A(t) = \eta \dot{M}_0^{\mathrm{SSE}}(t).\tag{4}$$

In this case, η^{-1}, whose unit is N·m/event, has an intuitive meaning, and can be interpreted as the SSE seismic moment required to trigger a single earthquake ($\geq M_c$). Therefore, we discuss η^{-1} frequently in the following sections. In Sections 3.1.3, 3.2.3, and 3.3.3, we have allowed τ and γ to take values other than 0 and 1, respectively, and examined whether the model was improved.

As can be seen from Equation 4, η, which is the proportionality constant between the seismicity rate (the number of earthquakes per unit time) and the SSE moment rate, does not directly depends on the SSE duration. In our model, SSEs with different durations can have the same η-value. If there are two SSEs with comparable moment rates and equal η-values, but different only in duration, our model expects the SSE with a longer duration to induce more earthquakes. This is because the time integral of the moment rate becomes larger when the duration is longer. Our model assumes the dependence of the number of induced earthquakes on time integral of the moment rate, rather than on the duration itself.

When estimating the ETAS parameters, it is convenient to multiply η by the SSE seismic moment M_0^{SSE}:

$$\eta' \equiv \eta M_0^{\mathrm{SSE}}\tag{5}$$

$$M_0^{\mathrm{SSE}} \equiv \int_0^T \dot{M}_0^{\mathrm{SSE}}(t)dt\tag{6}$$

where $t = 0$ is the time at which the ETAS analysis starts and $t = T$ is the time at which the analysis ends. If $\gamma = 1$, η' represents the number of earthquakes triggered by the SSE of the seismic moment M_0^{SSE}. Equation 4 can be rewritten as:

$$A(t) = \eta' \frac{\dot{M}_0^{\mathrm{SSE}}(t)}{M_0^{\mathrm{SSE}}}\tag{7}$$

If $\gamma \neq 1$, it is convenient to define η' as:

$$\eta' \equiv \eta \int_0^T \left\{ \dot{M}_0^{\text{SSE}}(t) \right\}^\gamma dt \tag{8}$$

$$A(t) = \eta' \frac{\left\{ \dot{M}_0^{\text{SSE}}(t) \right\}^\gamma}{\int_0^T \left\{ \dot{M}_0^{\text{SSE}}(t) \right\}^\gamma dt} \tag{9}$$

As in Equation 5, η' in Equation 8 represents the number of earthquakes triggered by the SSE of seismic moment M_0^{SSE}.

2.3.2. ETAS Parameter Estimation

Assuming a nonstationary Poisson process, we obtain the likelihood $L(\theta|X)$ of the ETAS model (Ogata, 1988) as

$$\log L(\theta|X) = \sum_{0 \leq t_i \leq T} \log \lambda(t_i) - \int_0^T \lambda(t) \, dt, \tag{10}$$

where θ is a set of the six ETAS parameters (μ, α, c, K, p, and η') and two additional parameters (τ and γ), and $X = \{(t_i, M_i) \,|\, 0 \leq t_i < T\}$ are the data (i.e., origin times and magnitudes of earthquakes). We assumed that the ETAS and additional parameters were non-negative.

To estimate the ETAS parameters, we followed the Bayesian ETAS parameter estimation approach proposed by Omi et al. (2015). We sampled the posterior probability distribution using the Markov chain Monte Carlo (MCMC) method. Based on Bayes' theorem, the posterior probability distribution $p(\theta|X)$ of the parameter set θ given the data X can be expressed using the likelihood $L(\theta|X)$ and the prior probability distribution $p(\theta)$ of the parameter set θ as follows:

$$p(\theta|X) \propto L(\theta|X) \cdot p(\theta). \tag{11}$$

We assumed a uniform prior probability distribution for the ETAS parameters, with μ in [0, 3], α and p in [0, 5], c and K in [0, 1], and η' in [0, 500]. These ranges were sufficiently broad to cover realistic values of the ETAS parameters. We used the uniform prior probability distribution $p(\theta)$ and the likelihood $L(\theta|X)$ to obtain the parameter set that maximizes the posterior probability distribution, that is, the maximum a posteriori (MAP) estimate. Because a uniform prior distribution does not change the posterior distribution, the posterior probability is solely proportional to the likelihood. Therefore, the MAP estimate is virtually identical to the maximum-likelihood estimate.

We evaluated the estimation uncertainty of the ETAS parameters by computing the 95% credible intervals (CIs) of the ETAS parameters from the MCMC samples. The merit of the Bayesian approach using the MCMC method (Omi et al., 2015) is that we can accurately assess the uncertainty of the ETAS parameters without approximating the posterior probability distribution and likelihood function. This approach also reveals the complex shape of the posterior probability distribution and the statistical correlations between the ETAS parameters (Omi et al., 2015). We used the Python library to implement the MCMC method. emcee is a pure-Python implementation of Goodman & Weare's affine-invariant MCMC ensemble sampler (Goodman & Weare, 2010). See https://emcee. readthedocs.io/en/stable/ and Foreman-Mackey et al. (2013) for details on emcee. We ran 30 chains of 30,500 steps and discarded the first 500 steps as a burn-in period. The autocorrelation times of the six ETAS parameters, a measure used to estimate the effective number of independent samples in each chain (Foreman-Mackey et al., 2013), ranged from 90 to 150 for all subsequent analyses. Therefore, our chains are much longer than 50 times the autocorrelation times ($\leq$7,500), which suggests that they are sufficiently converged (see https://emcee. readthedocs.io/en/stable/tutorials/autocorr/).

As described in Section 2.2, we used M 2.5 or greater earthquakes during the analysis periods (2006–2008 and 2009–2011) within the study regions (Figure 1) as data $X = \{(t_i, M_i) \,|\, 0 \leq t_i < T\}$. Furthermore, to consider increases in the seismicity rate due to the aftershock activity of earthquakes that occurred before the analysis periods, we also used earthquakes in the preceding year of each study period (i.e., 2005 and 2008) as a history part. We did not use the history part for the parameter optimization but only for considering the effects of the earthquakes before the study periods.

We used the same Bayesian method (Omi et al., 2015) and the same data (i.e., seismicity during the 3-year analysis periods) as the new model to estimate the parameters of the original ETAS model (Equation 1).

2.3.3. Model Selection

We compared the new model (Equation 2) with the original ETAS model (Equation 1) using Akaike's information criterion (AIC) (Akaike, 1974). We selected the model that minimized the AIC value as the best-fit model. The AIC is defined as:

$$AIC = -2 \log L(\theta|X) + 2k \tag{12}$$

where k denotes the number of adjusted parameters. We considered a model with a smaller AIC to be significantly better than a model with a larger AIC when the AIC difference between the two models was two or greater.

In Bayesian ETAS parameter estimation (Omi et al., 2015), defining the number of adjusted parameters (k) is not straightforward because prior conditions that restrict the parameters are used. However, as discussed in detail by Omi et al. (2015), if the standard deviation of the prior probability distribution is sufficiently large, which is true for our analysis (Section 2.3.2), one can disregard the influence of the prior conditions. Considering these facts, we used the number of the ETAS parameters to be estimated as k.

2.3.4. Transformed Time

The number of earthquakes $\Lambda(t)$ expected from the ETAS model from time t_0 to time t was obtained by integrating Equation 2:

$$\Lambda(t) = \int_{t_0}^{t} \lambda(t') \, dt' \tag{13}$$

Using Equation 13, we transformed the occurrence time of the ith earthquake t_i ($t_0 \leq t_i$) into a transformed time $\tau_i \equiv \Lambda(t_i)$ (Ogata, 1988).

If the analyzed seismicity can be well described by the ETAS model, the transformed time τ_i will follow a standard Poisson process (Ogata, 1988). Therefore, the plot of the cumulative number of observed earthquakes against the transformed time is expected to be linear with a slope of unity. Furthermore, the standard deviation σ of the number of earthquakes between time t_0 and the occurrence time of the ith earthquake t_i is given by:

$$\sigma = \sqrt{\tau_i}. \tag{14}$$

In Section 3, we use the above equations to compare the predictions of the new model with those of the original ETAS model.

2.4. Estimation of SSE Moment Rates

We used TDEFNODE (McCaffrey, 2009) to estimate the SSE moment rates. Note that the aim of this study is to develop a new statistical model of seismicity (Section 2.3); sophisticated estimation of the SSE slip evolution is beyond the scope of this study. TDEFNODE is a Fortran program that uses crustal deformation data to model fault locking and transient sources such as earthquakes, afterslip, and SSEs. For details on TDEFNODE, see McCaffrey (2009) and https://robmccaffrey.github.io/TDEFNODE/manual/tdefnode_manual.html. The source code is available at https://robmccaffrey.github.io/TDEFNODE/TDEFNODE.html.

TDEFNODE represents transient sources with a small number of parameters by assuming that the spatial distribution of the fault slip rates and their temporal evolution are independent. For simplicity, we assumed two-dimensional Gaussian functions for the spatial distribution of the slip rates on the plate interface as follows:

$$S_{\text{space}}(x, w) = \exp\left(-0.5 \cdot \left(\frac{d_w}{d_1}\right)^2\right) \cdot \exp\left(-0.5 \cdot \left(\frac{d_x}{d_2}\right)^2\right), \tag{15}$$

where w is the position in the direction of the plate motion, x is the position in the direction orthogonal to the plate motion, d_w and d_x are distances (km) in the w and x, directions, respectively, from the center of the slip distribution specified by parameters l_n and l_t, and d_1 and d_2 are the characteristic distances of the Gaussian functions.

We assumed a one-dimensional Gaussian function for the temporal evolution of the slip rates as follows:

$$S_{\text{time}}(t) = \exp\left(-0.5 \cdot \{(t - (T_0 + 3T_c))/T_c\}^2\right) \tag{16}$$

where T_c is the characteristic time scale that determines the duration of the temporal evolution of the slip rate, and T_0 is the time $3T_c$ before the time of the maximum slip rate $(T_0 + 3T_c)$ and can be considered as the start time of the SSE. Similarly, we regard $T_0 + 6T_c$ as the end time of the SSE.

The slip rate at position (x, w) and time t, is given by the product of the above two functions.

$$S(x, w, t) = A_m \cdot S_{\text{space}}(x, w) \cdot S_{\text{time}}(t), \tag{17}$$

where A_m is the maximum slip rate (mm/day).

We used Equation 17 and assigned slip rates to nodes on the plate interface. The nodes are distributed at intervals of tens of kilometers in the plate-motion and along-strike directions and are aligned along the iso-depth contours of the plate interface. The slip rates between the nodes were linearly interpolated. We then calculated the surface displacements caused by fault slip. See McCaffrey (2009) and https://robmccaffrey.github.io/TDEFNODE/manual/tdefnode_manual.html for details of the surface displacement calculation. We assumed a rigidity of 30 GPa and a Poisson's ratio of 0.25. The plate boundary surface geometry was based on Slab 2.0 (Hayes, 2018).

Eight fault parameters have to be estimated $(l_n, l_t, A_m, d_1, d_2, T_0, T_c,$ and slip azimuth $r_k)$. As described in Section 2.2, we used GNSS daily coordinates within 120-day time windows whose centers correspond to the center of each SSE occurrence period to estimate the fault parameters. As a preprocessing step, we fitted a linear function to the daily coordinates of the first 40 days and removed the linear trend from the coordinates within the entire time window. The SSE fault parameters were estimated by iteratively applying simulated annealing and grid search to minimize the sum of the reduced chi-square statistic (the sum of the squares of the weighted residuals normalized by the degrees of freedom) (McCaffrey, 2009; https://robmccaffrey.github.io/TDEFNODE/manual/tdefnode_manual.html). The weights are the inverse of the squared standard errors of the data.

We then computed the moment rate of the SSE $\dot{M}_{\text{SSE}}(t)$, by spatially integrating the spatiotemporal slip distribution. We used this moment rate to estimate the ETAS parameters (Sections 2.3.1 and 2.3.2). Uncertainty in the moment rate estimation affects the ETAS parameters, especially η, the proportionality constant between the SSE moment rate and the rate of SSE-induced earthquakes. Therefore, we examined moment rate uncertainty by bootstrap resampling (Efron & Tibshirani, 1994). We followed a procedure similar to that described by Okuda and Ide (2018). We randomly resampled the same number of GNSS stations used in slip inversion, allowing for duplication. We obtained 1,000 bootstrap samples. For each sample, we estimated the spatiotemporal slip distribution and moment rate. In Section 4.2, we use bootstrap samples and discuss the uncertainty of the ETAS parameters due to the uncertainty in the moment rate estimation.

3. Results

3.1. The August 2006 Southern Slow Slip Event

3.1.1. SSE Moment Rate Estimation

Figure 2 shows the slip distribution of the SSE that occurred in the south-central part of the Hikurangi Trench in August 2006. This SSE is centered at 40.4°S and 177.3°E, with a maximum slip of 310 mm and a horizontal dimension of approximately 50 km. The moment magnitude of the SSE, 1.89×10^{19} N·m (M_w 6.78), was comparable to that estimated by Wallace and Beavan (2010), M_w 6.8. The occurrence period of the SSE (i.e., the period from $\boldsymbol{T_0}$ to $\boldsymbol{T_0 + 6T_c}$) was from 25 August 2006, to 6 September 2006 (13 days). The eight fault parameters $(\boldsymbol{l_n, l_t, A_m, d_1, d_2, T_0, T_c,}$ and $\boldsymbol{r_k})$ are listed in the Supporting Information (Table S1 in Supporting Information S1). We note that there is a difference between the durations estimated by Wallace and Beavan (2010) (7 days) and this study (13 days). This is due to the difference in the methods to estimate them (see Section 2.1 and 2.4). Furthermore, SSE durations are generally difficult to estimate and have large errors (Okada et al., 2022).

Figure 2e shows the moment rate computed from the spatiotemporal evolution of the SSE slip rate, with a maximum value of $\boldsymbol{3.6 \times 10^{18}}$ N·m/day on August 30. In the next section, we use this moment rate function to estimate the ETAS parameters.
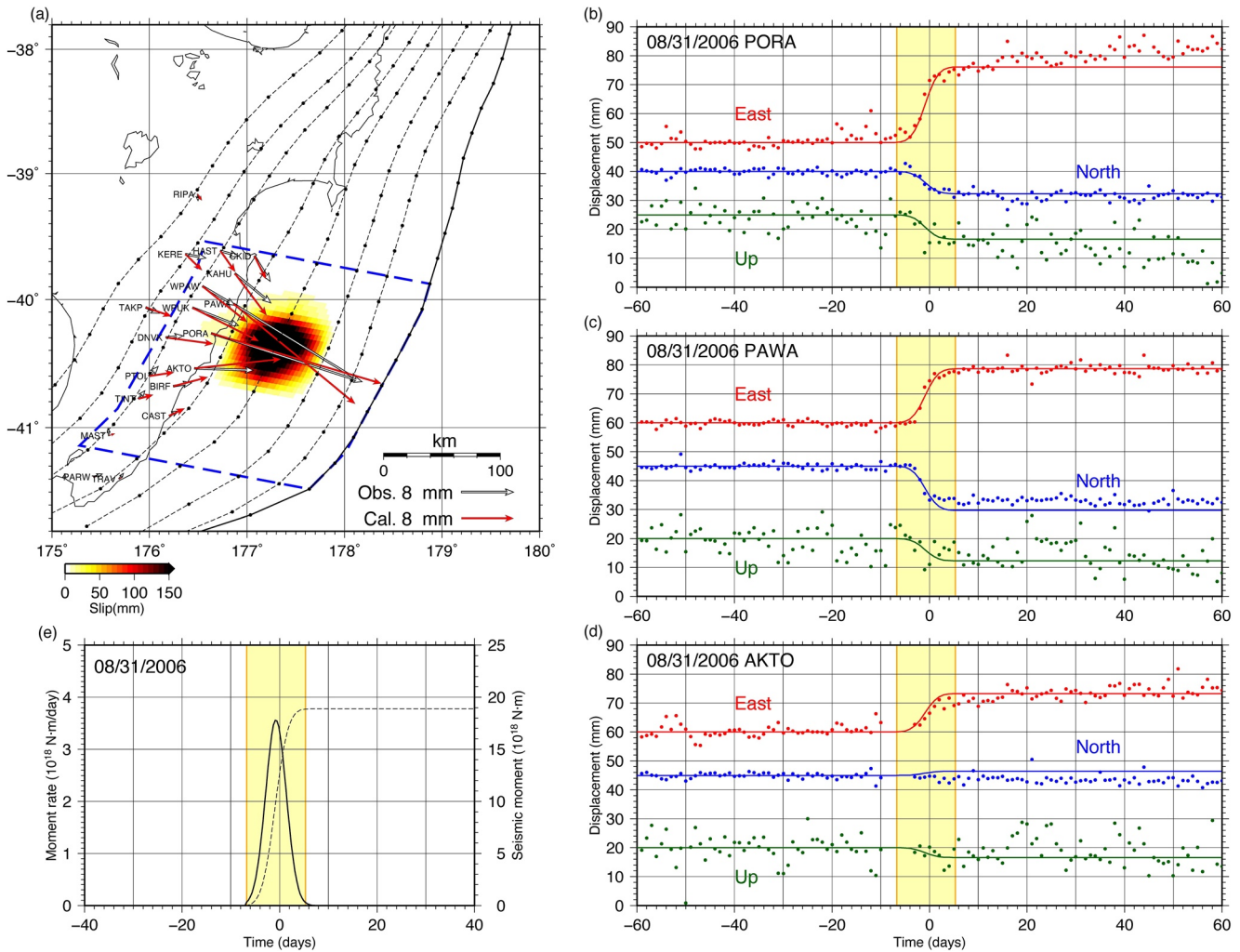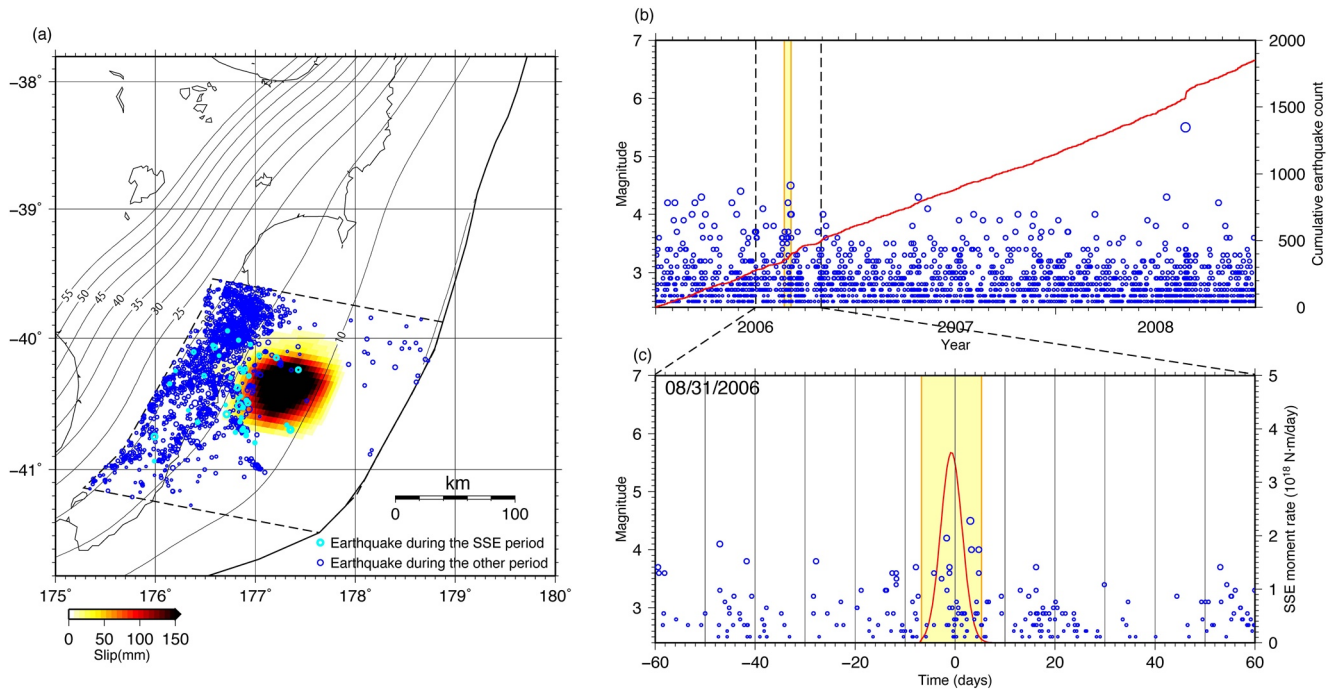
Figure 2. Slip distribution and moment rate function of the August 2006 southern slow slip event (SSE). (a) Slip distribution of the August 2006 southern SSE. White and red arrows indicate observed and calculated horizontal displacements, respectively. Black points indicate nodes used in TDEFNODE (Section 2.4). The blue dashed polygon indicates the study region used in the epidemic-type aftershock-sequence (ETAS) analysis. (b–d) Global navigation satellite system (GNSS) daily coordinates (colored points) of the three GNSS stations with the largest observed horizontal displacements (stations PORA, PAWA, and AKTO). The horizontal axis indicates the number of days from 31 August 2006. The colored solid lines show the temporal changes of the calculated displacements. Yellow areas indicate the SSE period that we estimated. (e) Moment rate and cumulative moment of the SSE (the solid and dashed lines, respectively). ETAS, epidemic-type aftershock-sequence; GNSS, global navigation satellite system; SSE, slow slip event.

3.1.2. ETAS Parameter Estimation and Transformed Time Calculation

Figure 3 shows the epicentral distribution and magnitude-time diagram of *M* 2.5 or larger earthquakes in the south-central part of the Hikurangi Trench from January 2006 to December 2008. We used these earthquakes to estimate the ETAS parameters. As pointed out by Nishikawa et al. (2021), the epicenters of the earthquakes (blue circles in Figure 3a) and the SSE slip are distributed in a complementary manner, with the SSE slip located on the updip side of the plate boundary. Most of the earthquakes are intraslab earthquakes (Nishikawa et al., 2021). The cyan circles in Figure 3a indicate the epicenters of the earthquakes that occurred during the period of the SSE (25 August 2006, to 6 September 2006). Like the other earthquakes (blue circles), these earthquakes were mainly located on the downdip side of the SSE slip area, with many of them distributed near the edge of the slip area.

We substituted the moment rate shown in Figure 2e into Equations 2 and 7. We then used the MCMC method and sampled the posterior probability distribution (Figure 4a). We obtained MAP estimates for the ETAS parameters (μ, α, c, K, p, and η') for seismicity shown in Figure 3. We used all the earthquakes in Figure 3b, regardless of whether they were background events or mainshock-aftershock-type earthquakes. The MAP estimate of η'
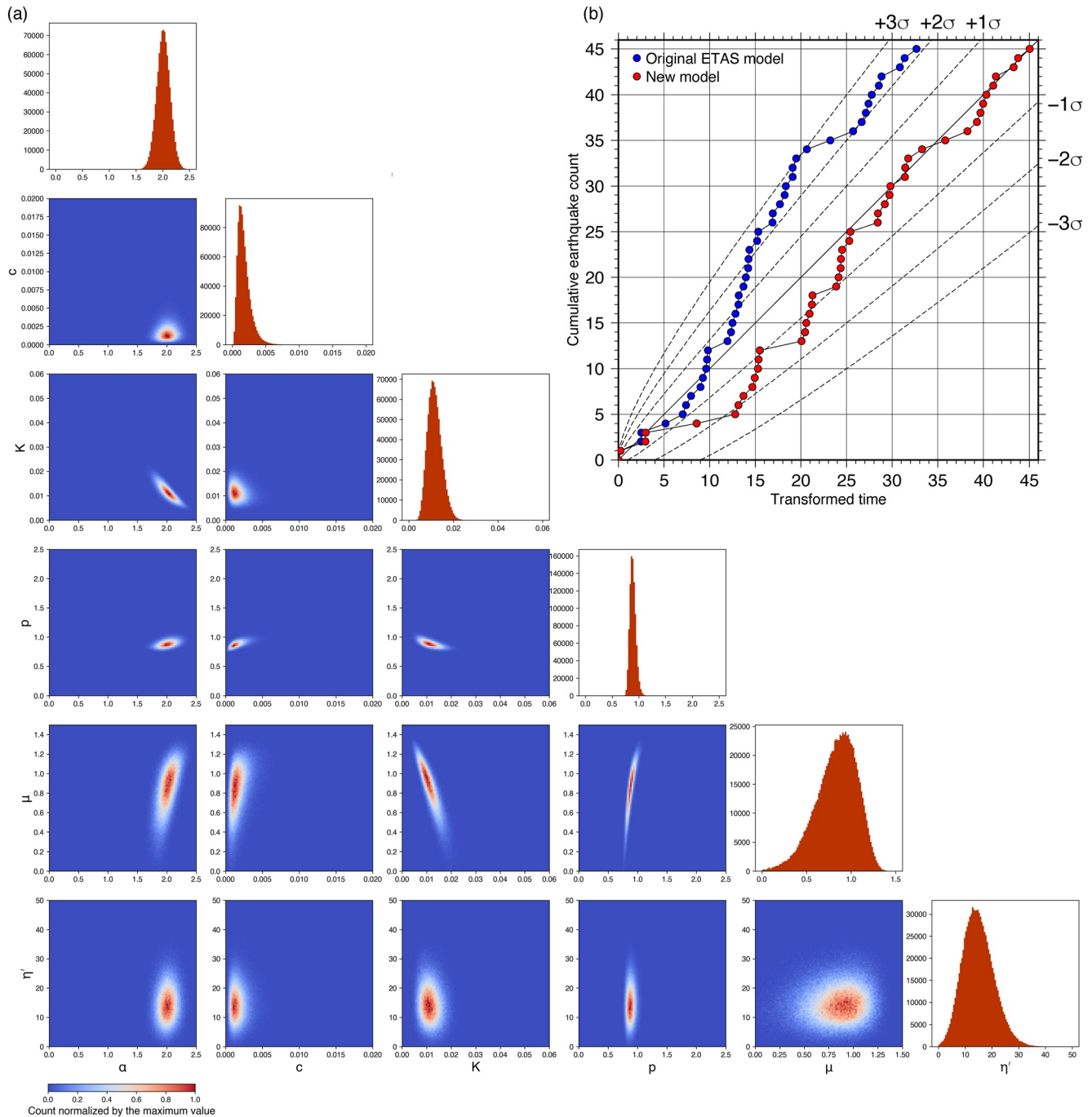
Figure 3. Seismicity in the south-central part of the Hikurangi Trench from January 2006 to December 2008. (a) Epicenters of earthquakes in the south-central part of the Hikurangi Trench from January 2006 to December 2008 (blue open circles). Cyan open circles are the epicenters of earthquakes during the period of the August 2006 southern slow slip event (SSE). The black area indicates the slip distribution of the August 2006 southern SSE. The dashed black polygon is the study region used for the ETAS analysis. The black contours indicate the depth contours of the upper surface of the Pacific Plate. (b and c) Magnitude-time diagrams of earthquakes used in the ETAS analysis. The yellow areas indicate the occurrence period of the SSE. The red line in (b) indicates the cumulative earthquake count. The red curve in (c) is the moment rate of the SSE. The horizontal axis in (c) indicates the number of days from 31 August 2006. ETAS, epidemic-type aftershock-sequence; SSE, slow slip event.

was $\eta' = 14$ events, with a 95% CI of 4.6–27 events. The MAP estimates for other ETAS parameters are listed in Table 1. We also listed the estimated parameters of the original ETAS model in Table 1. We used the MAP estimates to calculate the difference in AIC (ΔAIC) between the original ETAS model (Equation 1) and the new model (Equations 2 and 7). The resulting ΔAIC was -6.6, indicating that the new model was significantly better than the original ETAS model (Section 2.3.3). In addition, we used Equation 5 and calculated η^{-1} from η', finding η^{-1} to be 1.4×10^{18} N·m/event ($= M_w$ 6.0/event). This result implies that the moment magnitude of an SSE required to induce a single M 2.5 or greater earthquake is M_w 6.0.

Note that the MAP estimate of the **p**-value is less than one ($p = 0.86$; see Table 1). In this regime, the time integral of Omori-Utsu's aftershock law (i.e., the number of aftershocks) does not converge, and the ETAS model is in an unstable regime (Helmstetter & Sornette, 2002). Therefore, the MAP estimates cannot be extrapolated to longer periods outside of the analysis period. To avoid this problem, we reanalyzed the earthquake catalog assuming $p > 1$ in the prior probability distribution (see Text S2 in Supporting Information S1 for details). As a result, we found that the η'-value did not change significantly (from 14 to 16 events). This implies that the obtained η'-value is robust against changes in the p-value.

In Figure 4b, we compared the transformed time of the original ETAS model with that of the new model during the SSE period (25 August 2006, to 6 September 2006). The transformed time for the new model was calculated using the MAP estimates (Table 1). The transformed times for seismicity before and after the SSE are shown in Text S3 in Supporting Information S1. As explained in Section 2.3.4, if the seismicity is well described by these models, a plot of the cumulative number of observed earthquakes against the transformed time is expected to be linear with a slope of unity (the solid black line in Figure 4b). In the results of the original ETAS model (blue circles), near the end of the SSE (around the cumulative earthquake count of 30–45), the number of observed earthquakes was $+2\,\sigma$ (Equation 14) to $+3\,\sigma$ larger than the model prediction. In contrast, the prediction by the new model (red circles) was in the range of $-1\,\sigma$ to $+1\,\sigma$, suggesting that the observed values did not significantly exceed the predicted values near the end of the SSE. These results suggest that the predictions of the new

Figure 4. ETAS parameters estimated for the August 2006 southern slow slip event (SSE) and seismicity in the south-central part of the Hikurangi Trench from 2006 to 2008. (a) Marginal posterior probability distributions of the ETAS parameters (μ, α, c, K, p, and η'). (b) Transformed times for the original ETAS model and new model (blue and red circles, respectively) during the period of the SSE (25 August 2006, to 6 September 2006). ETAS, epidemic-type aftershock-sequence; SSE, slow slip event.

model are superior to those of the original ETAS model. However, we note that the new model overpredicted the number of earthquakes near the start of the SSE (around a cumulative earthquake count of 0–5), suggesting that fewer earthquakes occurred than expected from the assumed linear relationship between the SSE moment rate and seismicity rate (Equation 4). This tendency is also evident in Figure 3c, where the first half of the SSE period (before −2 d) is characterized by fewer earthquakes than the second half. This over-prediction may be due to our simple assumption of linearity or the uncertainty in the SSE moment rate.

Table 1
*Maximum A Posteriori Estimates of the Epidemic-Type Aftershock-Sequence (ETAS) Model Parameters*

Slow slip event (SSE)	ETAS model	μ (events/day)	α	c (days)	K (events/day^(1-p))	p	η' (events)
2006 southern SSE	Original	0.71	2.0	1.2×10^{-3}	1.3×10^{-2}	0.85	N/A
	Modified	0.81	2.0	1.1×10^{-3}	1.1×10^{-2}	0.86	14
2011 southern SSE	Original	1.2	1.5	5.4×10^{-3}	1.6×10^{-2}	0.98	N/A
	Modified	1.5	1.6	7.7×10^{-3}	6.8×10^{-3}	1.2	62
2008 northern SSE	Original	1.2	1.7	9.2×10^{-3}	1.9×10^{-2}	0.97	N/A
	Modified	1.2	1.7	9.3×10^{-3}	1.9×10^{-2}	0.97	6.5

3.1.3. Estimation of Lag Time and Power Exponent

In this section, we examine the functional form (Equation 3) that relates the SSE moment rate to the seismicity rate. Specifically, we did not fix the lag time τ and power exponent γ at $\tau = 0$ or $\gamma = 1$, but allowed them to vary. For simplicity, we conducted the analyses independently for τ and γ; when τ was allowed to vary, we fixed $\gamma = 1$, and when γ was allowed to vary, we fixed $\tau = 0$.

As shown below, we found that the marginal likelihood distribution for the lag time τ is significantly multi-modal. This made a sampling of the MCMC method using the Python package emcee's algorithm (Goodman & Weare, 2010) technically difficult. In other words, it was difficult for samplers to get out of the local minima of the posterior probability distribution. Therefore, we conducted a grid search with respect to the lag time τ (Figure 5a) and obtained the maximum likelihood estimates. In the Bayesian parameter estimation of this study (Section 2.3.2), the prior probability distributions were assumed to be uniform distributions. Therefore, the MAP estimates of our Bayesian approach and the maximum likelihood estimates obtained here are identical, and the results are the same for both methods. We performed a similar analysis for the power exponent γ, which is another additional parameter of our model.

Figure 5a shows the change in ΔAIC when the lag time τ was changed from 0 to 30 days in 0.1-day increments. The maximum likelihood estimates of the ETAS parameters (μ, α, c, K, p, and η') that were used to calculate ΔAIC were estimated using the Nelder–Mead method (Nelder & Mead, 1965). The results showed a minimum
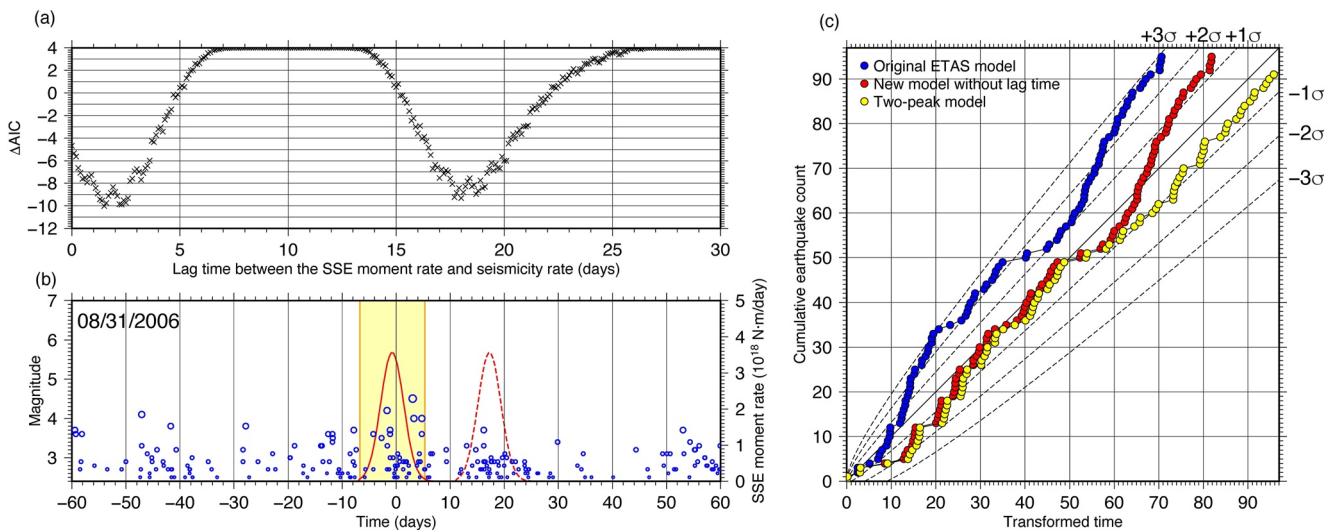
Figure 5. Estimation of lag time between the SSE moment rate and seismicity rate for the August 2006 southern SSE. (a) Change in ΔAIC with lag time τ varied from 0 to 30 days. (b) Magnitude-time diagram of earthquakes within 60 days before or after the period of the SSE. The yellow area indicates the period when the SSE occurred. The red curve is the moment rate of the SSE, and the dashed red curve is the moment rate of the SSE shifted by +18.0 days. The horizontal axis shows the number of days from 31 August 2006. (c) Transformed times for the original ETAS model, new model without lag time, and two-peak model (blue, red, and yellow solid circles, respectively) during the period of the SSE (from 25 August 2006, to 6 September 2006; cumulative earthquake counts less than 46) and after it (from 7 September 2006 to 24 September 2006). ETAS, epidemic-type aftershock-sequence; SSE, slow slip event.

ΔAIC (= −10.0) at τ = 1.5 d, indicating a significant increase in the seismicity rate almost concurrent with the SSE. A comparable decrease in ΔAIC (= −9.3) was observed at τ = 18.0 d. This indicates that approximately 18 d after the SSE, there was another anomalous increase in the seismicity rate that could not be explained by the original ETAS model (Figure 5b). In the Hikurangi Trench, lag times between SSEs and the associated seismicity are sometimes observed (Nishikawa et al., 2021; Shaddox & Schwartz, 2019). Nishikawa et al. (2021) proposed that post-SSE fluid migration may trigger an increase in the seismicity rate after an SSE. Based on their hypothesis, we considered the delayed anomalous seismicity shown in Figures 5a and 5b to be a manifestation of the post-SSE earthquake-triggering effect.

In order to account for both the co-SSE and post-SSE seismicity rate increases (Figure 5b; Nishikawa et al., 2021), we assumed that the seismicity rate $A(t)$ of earthquakes induced by the August 2006 southern SSE is expressed as follows:

$$A(t) = \eta\left\{\dot{M}_{\text{SSE}}(t) + \dot{M}_{\text{SSE}}(t - \tau_0)\right\},\qquad(18)$$

where τ_0 is set to 18.0 days. When we used Equation 18, ΔAIC decreased to −18.8, indicating that the model that considered both the co-SSE and post-SSE seismicity rate increases was the best. In Figure 5c, we compare the transformed times (25 August 2006, to 24 September 2006) of the original ETAS model, the new model without lag time (Equation 4), and the model with both the co-SSE and post-SSE seismicity rate increases (hereafter referred to as the two-peak model). In the two-peak model (yellow circles), after the SSE (after 6 September 2006; cumulative earthquake counts larger than 46), the difference between the observed and predicted earthquake counts remained in the range of −1 σ to +1 σ, suggesting good agreement with the observed and predicted values. By contrast, for the original ETAS model (blue circles) and the model without lag time (red circles), the observed values eventually exceeded the predictions by approximately +3 σ and +1.5 σ, respectively. These results suggest that the predictions of the two-peak model are better than those of the other models.

Next, we examined the change in ΔAIC when the power exponent γ (Equation 3) was varied from 0.5 to 4.0 in increments of 0.1 (Figure S2a in Supporting Information S1). Although ΔAIC = −6.6 at γ = 3.5 was the smallest in Figure S2a in Supporting Information S1, this was comparable to the ΔAIC (= −6.6; see Section 3.1.2) with γ fixed at 1.0. This result suggests that allowing γ to vary does not significantly improve our model.

3.2. The June 2011 Southern Slow Slip Event

3.2.1. SSE Moment Rate Estimation

Figure 6 shows the slip distribution of the June 2011 SSE in the south-central part of the Hikurangi Trench. This SSE is centered at 40.5°S and 177.1°E, with a maximum slip of 120 mm, and extends more than 100 km in the south-southwest to north-northeast direction. Compared to the August 2006 southern SSE in Figure 2a, the June 2011 southern SSE is characterized by a slip distribution that extends to 41°S.

The SSE moment calculated from the slip distribution was 1.53×10^{19} N·m (M_w 6.72). This magnitude was comparable to that estimated by Wallace et al. (2012), M_w 6.8. The occurrence period of the SSE (i.e., T_0 to $T_0 + 6T_c$) was from 15 June 2011, to 20 July 2011 (36 days). The eight estimated TDEFNODE parameters, $l_n, l_t, A_m, d_1, d_2, T_0, T_c,$ and r_k are listed in the Supporting Information (Table S1 in Supporting Information S1). Figure 6e shows the moment rate computed from the spatiotemporal evolution of the SSE slip rate, with a maximum value of 0.8×10^{18} N·m/day on July 5. In the next section, we use this moment rate function to estimate the ETAS parameters.

In Figure 6d, the observed eastward displacement (red points) at station CAST, located near the southern edge of the slip distribution (40.9°S), appears to have preceded the modeled displacement (red curve). Wallace et al. (2012) pointed out that this SSE can be divided into successive southern and northern subevents. Because of the simplicity of our modeling (see Section 2.4), our fault model could not represent such a complex spatiotemporal slip evolution. This probably caused the discrepancy between the observed and calculated values (Figure 6d). In Section 4.2, we discuss how these two subevents affect the MAP estimate of η and the ΔAIC value.

#### 3.2.2. ETAS Parameter Estimation and Transformed Time Calculation

Figure 7 shows the epicentral distribution and magnitude-time diagram of M 2.5 or larger earthquakes, in the south-central part of the Hikurangi Trench from January 2009 to December 2011. We used these earthquakes
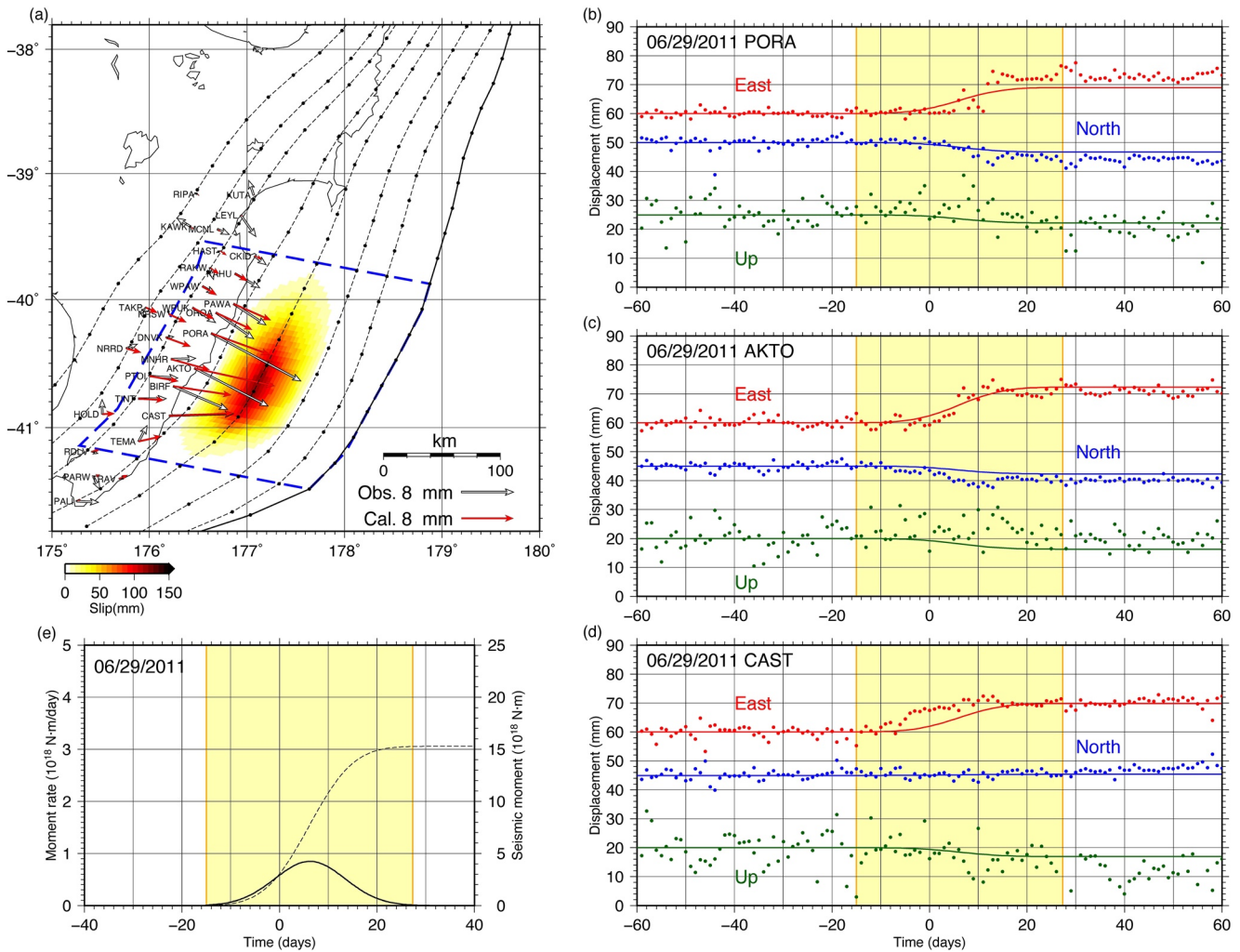
Figure 6. Slip distribution and moment rate function of the June 2011 southern SSE. (a) Slip distribution of the June 2011 southern SSE. White and red arrows indicate observed and calculated horizontal displacements, respectively. Black points indicate nodes used in TDEFNODE. The dashed blue polygon indicates the study region used in the epidemic-type aftershock-sequence analysis. (b–d) GNSS daily coordinates (colored points) of the three GNSS stations with the largest observed horizontal displacements (stations PORA, AKTO, and CAST). The horizontal axis indicates the number of days from 29 June 2011. The colored solid lines show the temporal changes of the calculated displacements. Yellow areas indicate the SSE period that we estimated. (e) Moment rate and cumulative moment of the SSE (solid and dashed lines, respectively). ETAS, epidemic-type aftershock-sequence; GNSS, global navigation satellite system; SSE, slow slip event.

to estimate the ETAS parameters. Similar to the August 2006 southern SSE (Figure 3a), the epicenters of the earthquakes (blue circles in Figure 7a) and the SSE slip are distributed in a complementary manner, with the SSE slip located on the updip side of the plate boundary. The cyan circles in Figure 7a indicate the epicenters of earthquakes that occurred during the SSE period (15 June 2011, to 20 July 2011). Like the other earthquakes (blue circles), these earthquakes are mainly located on the downdip side of the SSE slip area, with some of them distributed near the edge of the slip area.

We substituted the moment rates in Figure 6e into Equations 2 and 7. We then sampled the posterior probability distribution and obtained the MAP estimates of the ETAS parameters (μ, α, c, K, p, and η') for the seismicity shown in Figure 7 using the MCMC method (Figure 8a). We used all the earthquakes in Figure 7b, regardless of whether they were background events or mainshock-aftershock-type earthquakes. The MAP estimate for η' is $\eta' = 62$ events, with a 95% CI from 40 to 88 events. The MAP estimates for the other ETAS parameters are listed in Table 1. We used the MAP estimates to calculate ΔAIC. The resulting ΔAIC was -30.4, indicating that the new model was significantly better than the original ETAS model. In addition, using Equation 5, we calculated η^{-1} from η' to obtain $\eta^{-1} = 2.5 \times 10^{17}$ N·m/event ($= M_w$ 5.5/event). This result implies that the moment magnitude
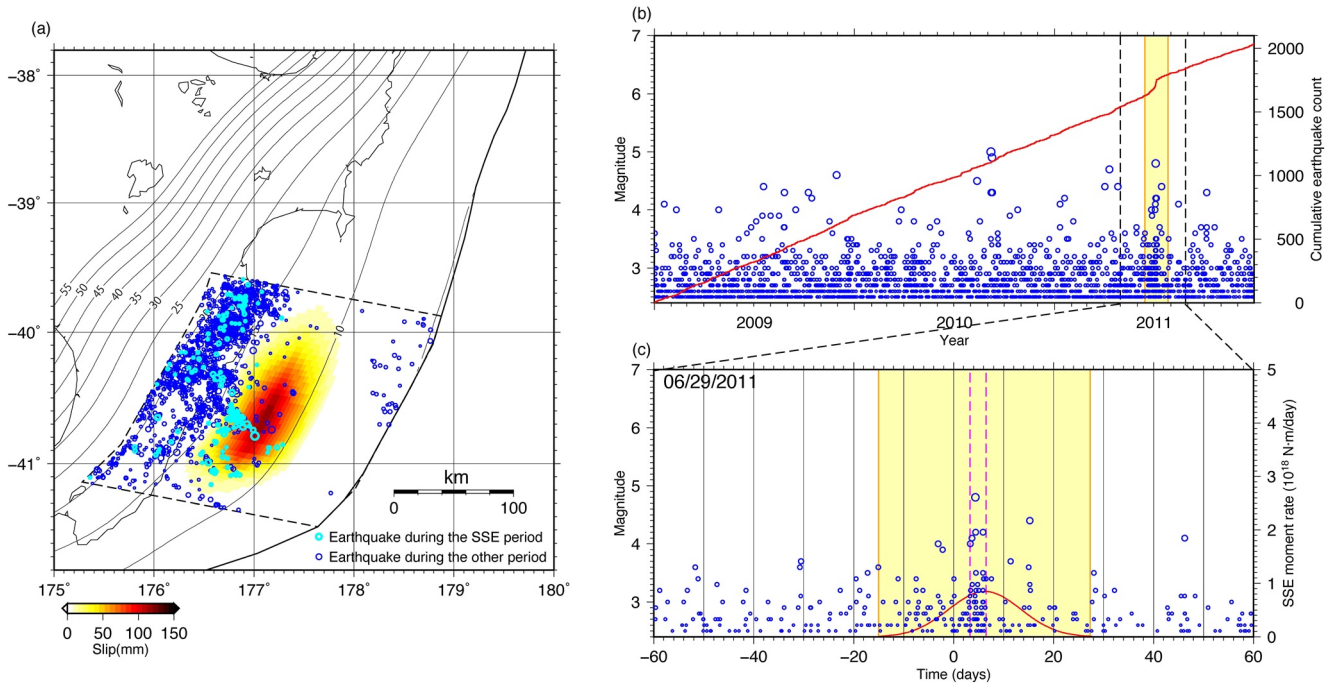
Figure 7. Seismicity in the south-central part of the Hikurangi Trench from January 2009 to December 2011. (a) Epicenters of earthquakes in the south-central part of the Hikurangi Trench from January 2009 to December 2011 (blue open circles). Cyan open circles are the epicenters of earthquakes during the period of the June 2011 southern SSE. The reddish region indicates the slip distribution of the June 2011 southern SSE. The black dashed polygon is the study region used for the ETAS analysis. The black contours indicate the depth contours of the upper surface of the Pacific Plate. (b and c) Magnitude-time diagrams of earthquakes used in the ETAS analysis. Yellow areas indicate the occurrence period of the SSE. The red line in (b) indicates the cumulative earthquake count. The red curve in (c) is the moment rate of the SSE. The horizontal axis in (c) indicates the number of days from 29 June 2006. The two dashed magenta lines in (c) indicate the period when the observed number of earthquakes substantially exceeded the ETAS prediction (see also Figure 8b). ETAS, epidemic-type aftershock-sequence; SSE, slow slip event.

of an SSE required to induce a single M 2.5 or greater earthquake is M_w 5.5, which is smaller than the estimate for the August 2006 southern SSE (M_w 6.0/event).

In Figure 8b, we compare the transformed time of the new model with that of the original ETAS model during the SSE period (15 June 2011, to 20 July 2011). In the result of the original ETAS model (blue solid circles), the number of observed earthquakes was approximately +5 σ (Equation 14) larger than the model prediction (black solid line in Figure 4b) at the end of the SSE period. In contrast, the results of the new model (red solid circles) showed an approximately +1 σ deviation from the model prediction, suggesting that the observed values did not significantly exceed the predicted values. These results suggest that the predictions of the new model are better than those of the original ETAS model. However, the new model did not perfectly predict the observed seismicity. During the period when the cumulative earthquake count was between 65 and 125 (between the two dashed magenta lines in Figures 7c and 8b), the observed earthquake count (60 events) was approximately twice the predicted value (28 events). This indicates that the observed earthquake occurrence rate substantially exceeded the seismicity rate expected from the linear relationship between the SSE moment rate and the SSE-induced seismicity rate (Equation 4). The assumption that the seismicity rate of SSE-induced earthquakes is proportional to the SSE moment rate may be too simplistic to describe the seismicity during this period. Furthermore, the influence of SSEs on aftershock productivity may not be negligible for this seismicity (Equation 2; Section 2.3.1). We further discuss this possibility in Section 4.3.

3.2.3. Estimation of Lag Time and Power Exponent

We examined the functional form (Equation 3) that relates the SSE moment rate to the seismicity rate. We allowed the lag time τ and power exponent γ to vary. The results are shown in Figures S2b and S3a in Supporting Information S1, respectively. For lag time τ (Figure S3a in Supporting Information S1), ΔAIC was minimized when $\tau = 0$, indicating that non-zero lag time did not improve the model. For the power exponent γ (Figure S1a in Supporting Information S1), the ΔAIC ($= -29.1$) was the smallest at $\gamma = 2.1$. However, it was larger than the ΔAIC ($= -30.4$) for the model with γ fixed at 1.0, indicating that a variable power exponent also did not improve the model.
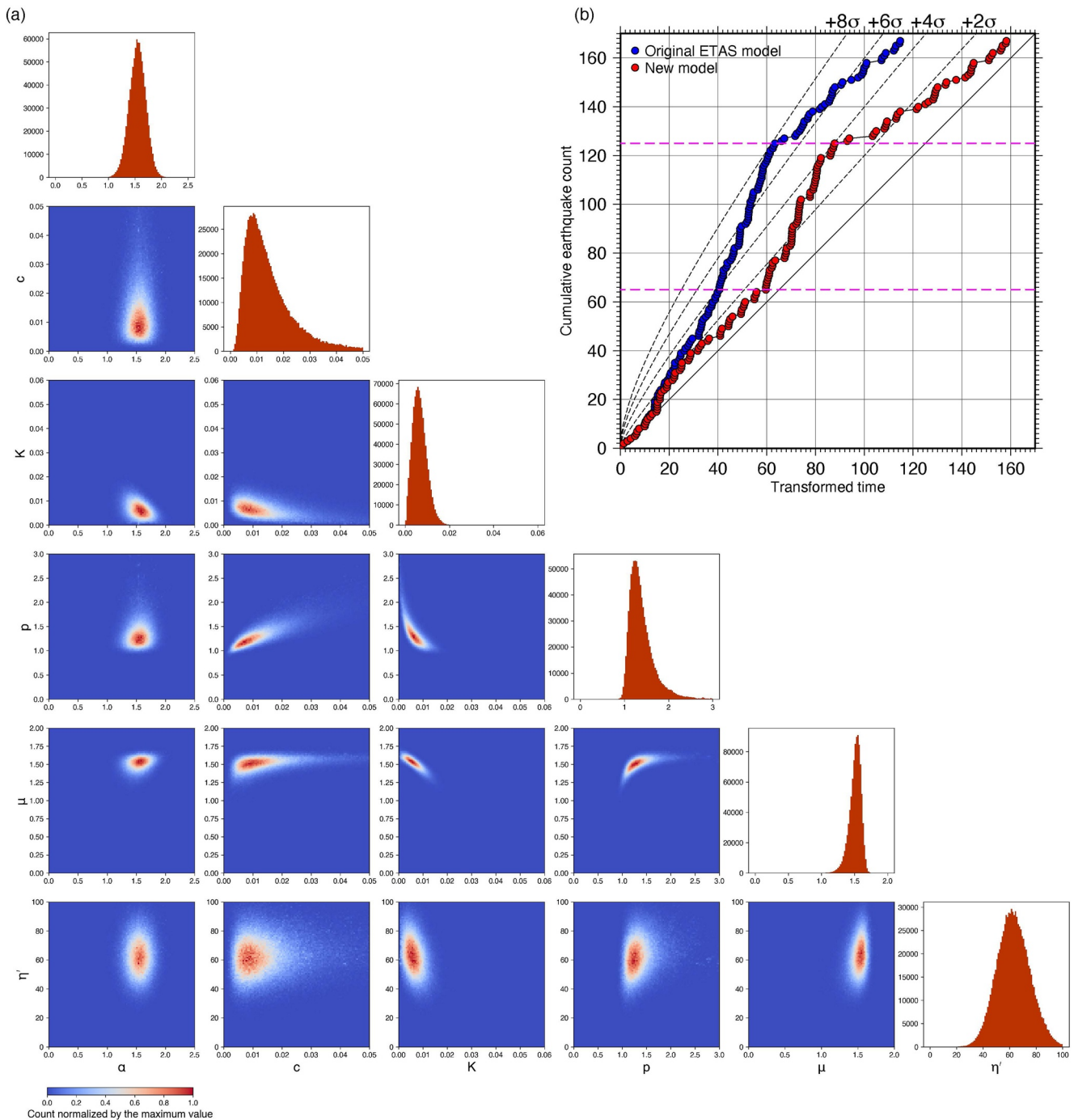
Figure 8. ETAS parameters estimated for the September 2011 southern SSE and seismicity in the south-central part of the Hikurangi Trench from 2009 to 2011. (a) Marginal posterior probability distributions of the ETAS parameters (μ, α, c, K, p, and η'). (b) Transformed times for the original ETAS model and new model (blue and red circles, respectively) during the period of the SSE (15 June 2011, to 20 July 2011). The magenta dashed lines in (b) indicate the period (the cumulative earthquake count from 65 to 125) when the observed number of earthquakes substantially exceeded the ETAS prediction (see also Figure 7c). ETAS, epidemic-type aftershock-sequence; SSE, slow slip event.

3.3. The March 2008 Northern Slow Slip Event

3.3.1. SSE Moment Rate Estimation

Figure 9 shows the slip distribution of the March 2008 SSE in the north-central part of the Hikurangi Trench. This SSE is centered at 39.2°S and 177.8°E, with a maximum slip of 50 mm and a horizontal dimension of several
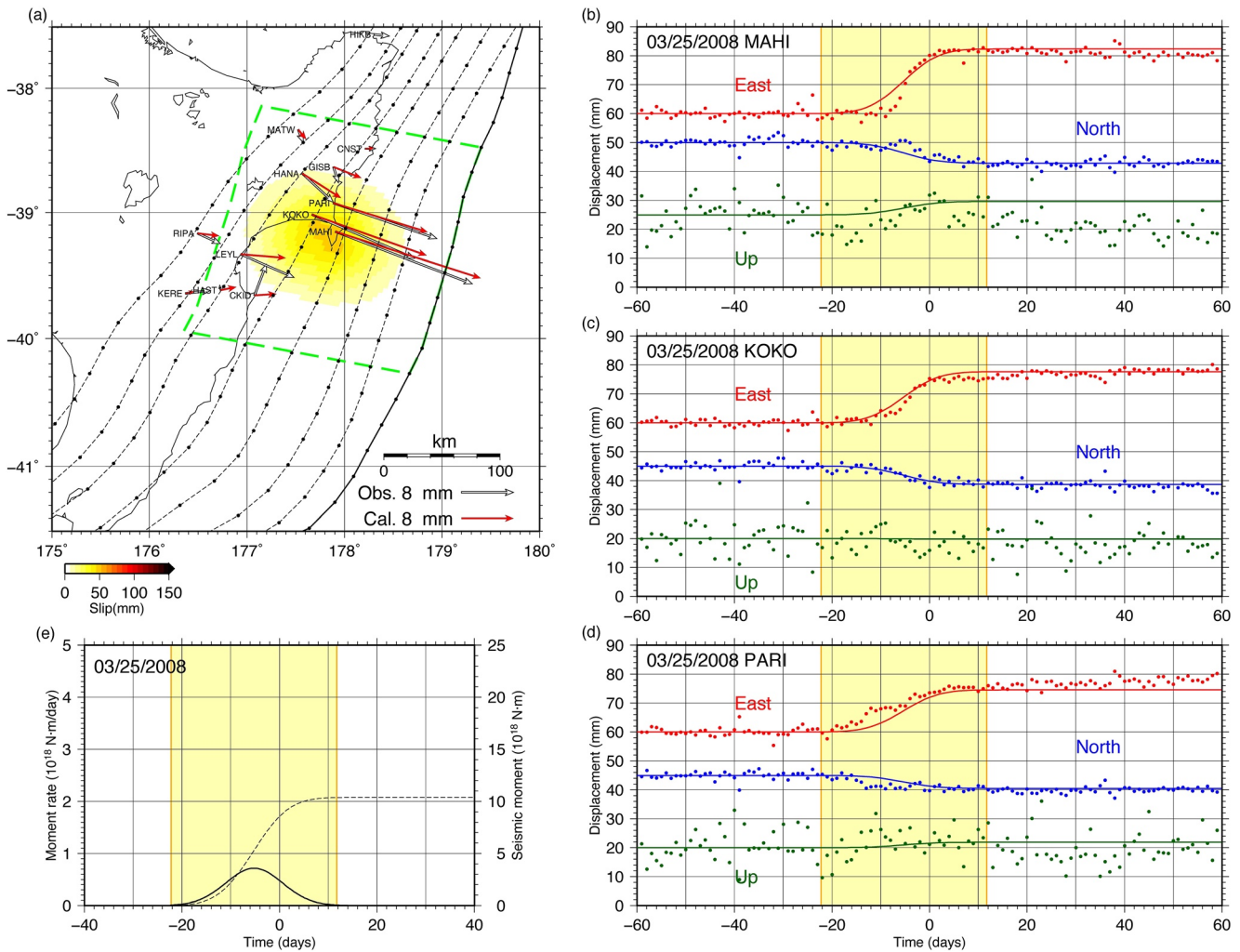
Figure 9. Slip distribution and moment rate function of the March 2008 northern SSE. (a) Slip distribution of the March 2008 northern SSE. White and red arrows indicate observed and calculated horizontal displacements, respectively. Black points indicate nodes used in TDEFNODE (Section 2.4). The green dashed polygon indicates the study region used in the ETAS analysis. (b–d) GNSS daily coordinates (colored points) of the three GNSS stations with the largest observed horizontal displacements (stations MAHI, KOKO, and PARI). The horizontal axis indicates the number of days from 25 March 2008. The colored solid lines show the temporal changes of the calculated displacements. Yellow areas indicate the SSE period that we estimated. (e) Moment rate and cumulative moment of the SSE (the solid and dashed lines, respectively). ETAS, epidemic-type aftershock-sequence; GNSS, global navigation satellite system; SSE, slow slip event.

tens of kilometers. The moment of SSE calculated from the slip distribution is 1.04×10^{19} N·m (M_w 6.61). This moment magnitude was comparable to that estimated by Wallace & Beavan. (2010), M_w 6.7. The occurrence period of the SSE (i.e., T_0 to $T_0 + 6T_c$) was from 3 March 2008, to 8 April 2008 (37 days). The eight estimated TDEFNODE parameters, $l_n, l_t, A_m, d_1, d_2, T_0, T_c$, and r_k, are listed in the Supporting Information (Table S1 in Supporting Information S1). Figure 9e shows the moment rate computed from the spatiotemporal evolution of the SSE slip rate, with a maximum value of 0.7×10^{18} N·m/day on March 20. In the next section, we use this moment rate function to estimate the ETAS parameters.

3.3.2. ETAS Parameter Estimation and Transformed Time Calculation

Figure 10 shows the epicentral distribution and magnitude-time diagram of M 2.5 or larger earthquakes in the north-central part of the Hikurangi Trench from January 2006 to December 2008, which we used to estimate the ETAS parameters. In contrast to the southern SSEs of August 2006 and June 2011 (Figures 3a and 7a), the epicenters of the earthquakes (green circles in Figure 10a) substantially overlapped with the slip area of the northern SSE in March 2008. Most of the earthquakes are intraslab earthquakes (Nishikawa et al., 2021; Warren-Smith et al., 2019; Yarce et al., 2019). The light green circles in Figure 10a indicate the epicenters of
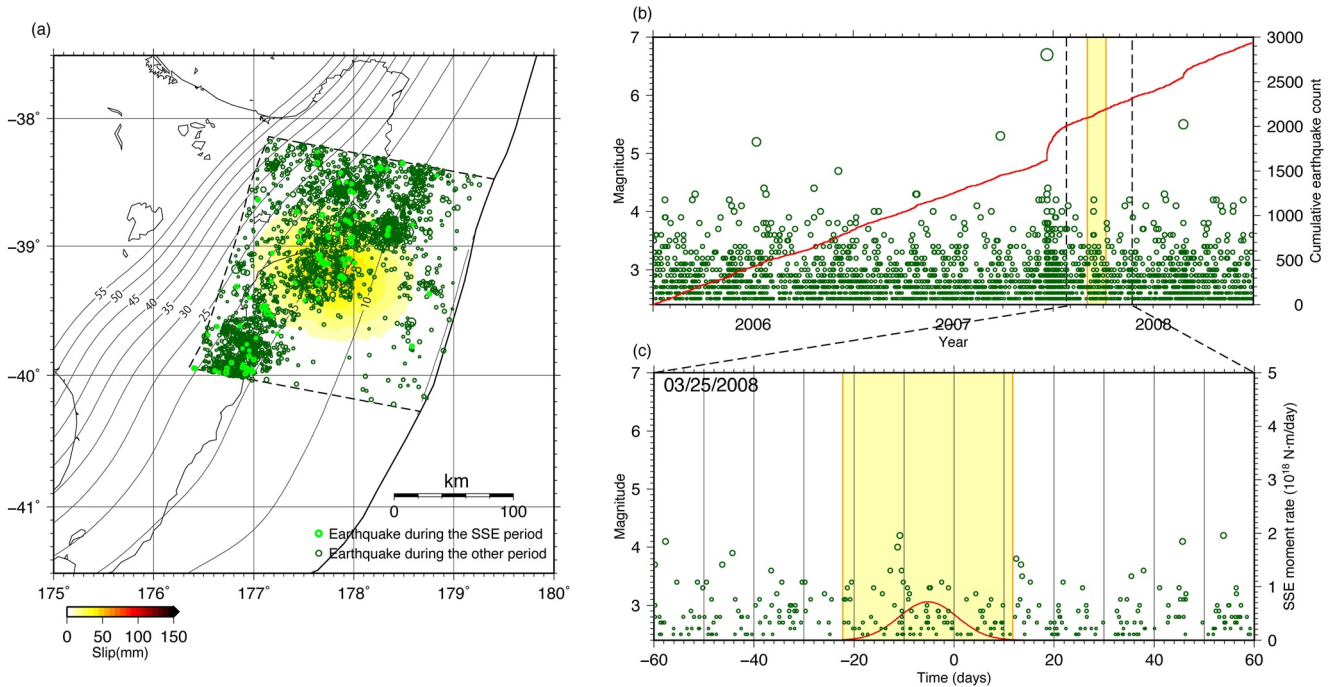
Figure 10. Seismicity in the north-central part of the Hikurangi Trench from January 2006 to December 2008. (a) Epicenters of earthquakes in the north-central part of the Hikurangi Trench from January 2006 to December 2008 (green open circles). Light green open circles are the epicenters of earthquakes during the period of the March 2008 northern SSE. The yellow-shaded region indicates the slip distribution of the March 2008 northern SSE. The black dashed polygon is the study region used for the ETAS analysis. Black contours indicate the depth contours of the upper surface of the Pacific Plate. (b and c) Magnitude-time diagrams of earthquakes used in the ETAS analysis. Yellow areas indicate the occurrence period of the SSE. The red line in (b) indicates the cumulative earthquake count. The red curve in (c) is the moment rate of the SSE. The horizontal axis in (c) indicates the number of days from 25 March 2008. ETAS, epidemic-type aftershock-sequence; SSE, slow slip event.

earthquakes that occurred during the SSE period (3 May 2008, to 8 April 2008). The epicenters of these earthquakes also overlapped with the slip area of the SSE.

We substituted the moment rates in Figure 9e into Equations 2 and 7. We then used the MCMC method to obtain the marginal posterior probability distributions (Figure 11a) and MAP estimates (Table 1) of the ETAS parameters (μ, α, c, K, p, and η') for the seismicity shown in Figure 10. We used all the earthquakes in Figure 10b, regardless of whether they were background events or mainshock-aftershock-type earthquakes.

The MAP estimates for η' and η^{-1} were $\eta' = 6.5$ events and $\eta^{-1} = 1.6 \times 10^{18}$ N·m/event (= M_w 6.1/event), respectively. The estimated η'-value was smaller than those estimated for the southern SSEs in August 2006 and June 2011. Furthermore, we found the ΔAIC for the March 2008 SSE to be 1.5, indicating no significant improvement over the original ETAS model. These results suggest that the seismicity-triggering effect of the northern SSE in March 2008 was insignificant. We confirmed that the minimum magnitude used in this analysis (M_c = 2.5 or 2.6; Section 2.2) did not affect this result; with a minimum magnitude of M 2.6, ΔAIC was 1.1.

Note that the obtained p-value is less than one ($p = 0.97$; see Table 1). Therefore, the ETAS model is in an unstable regime (Helmstetter & Sornette, 2002; Section 3.1.2). In Text S2 in Supporting Information S1, we reanalyzed the earthquake catalog assuming $p > 1$ in the prior probability distribution (see Text S2 in Supporting Information S1 for details). As a result, we found that the assumption did not change the η'-value significantly (from 6.5 to 8.0 events).

In Figure 11b, we compare the transformed time of the new model with that of the original ETAS model during the SSE occurrence period (3 March 2008, to 8 April 2008). The predictions by both models were in the range of $-1\,\sigma$ to $+1\,\sigma$. This indicates that there was no significant difference between the predictions of the original and new models.

3.3.3. Estimation of the Lag Time and Power Exponent

We examined the functional form (Equation 3) relating the SSE moment rate to the seismicity rate, with the lag time τ and power exponent γ allowed to vary. The results are shown in Figures S2c and S3b in Supporting Information S1. With regard to lag time τ (Figure S3b in Supporting Information S1), ΔAIC was larger than 2 for
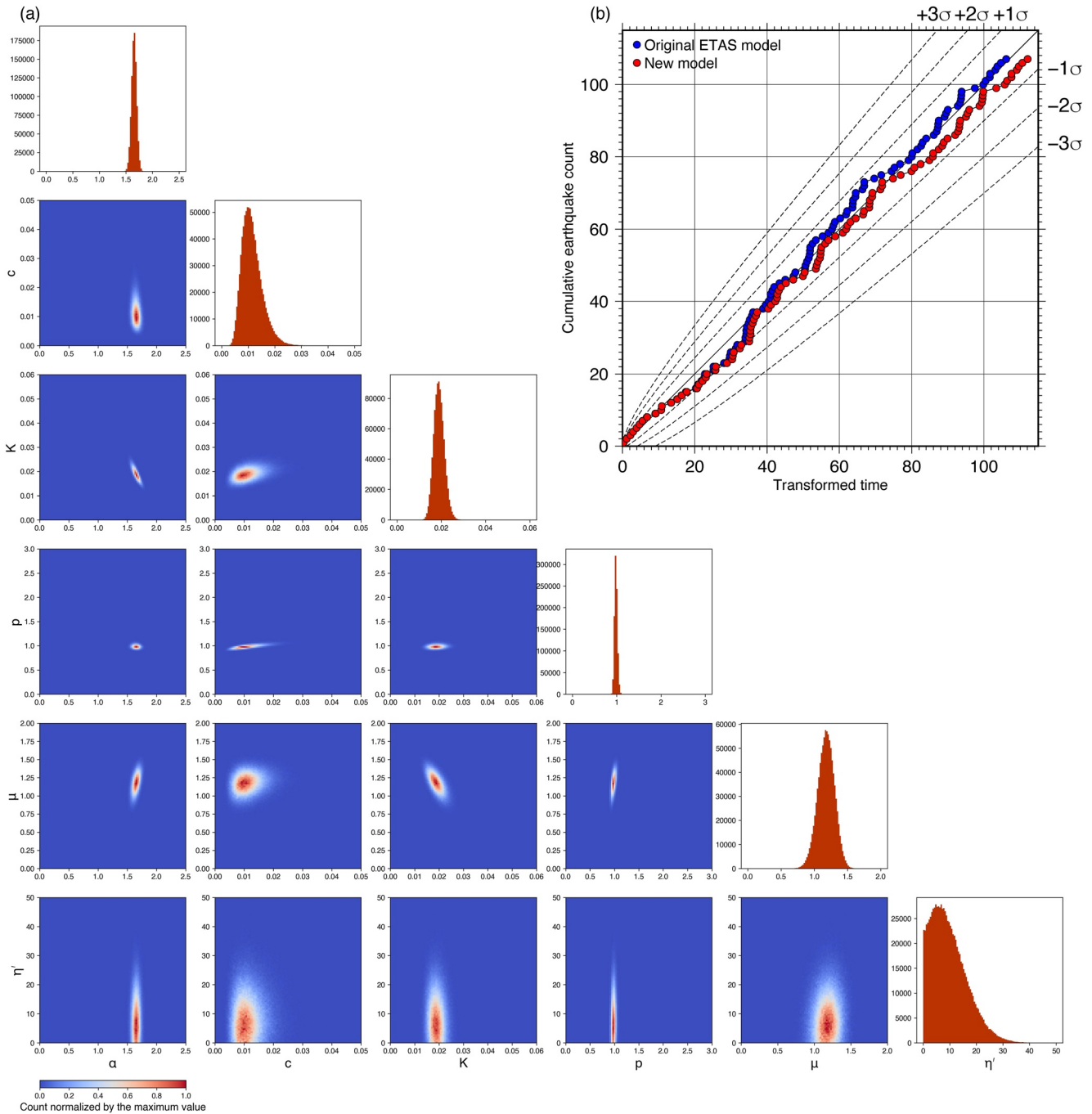
Figure 11. ETAS parameters estimated for the March 2008 northern SSE and seismicity in the north-central part of the Hikurangi Trench from 2009 to 2011. (a) Marginal posterior probability distributions of the ETAS parameters (μ, α, c, K, p, and η'). (b) Transformed times for the original ETAS model and new model (blue and red circles, respectively) during the SSE period (3 March 2008, to 8 April 2008). ETAS, epidemic-type aftershock-sequence; SSE, slow slip event.

all values of τ between 0 and 30 days, indicating that the original ETAS model was significantly better than the model with lag time. Similarly, for the power exponent γ (Figure S2c in Supporting Information S1), ΔAIC was larger than 2 for all values of γ from 0.5 to 4.0, indicating that the original ETAS model was significantly better than the model with a variable power exponent. These results suggest that the seismicity-triggering effect of the northern SSE in March 2008 was insignificant.

4. Discussion

4.1. Differences in Seismicity-Triggering Effects Between the Three SSEs

The results in Section 3 show that the seismicity-triggering effects of the SSEs in the Hikurangi Trench vary significantly. For the southern SSE in August 2006, we observed significant co-SSE and post-SSE seismicity-triggering effects (Figure 5), and the model that accounted for both effects (Equation 18) was the best. For the southern SSE in June 2011, the model that considers the co-SSE seismicity-triggering effect of ($\tau = 0$) was the best model, with the post-SSE effect being insignificant (Figure S3a in Supporting Information S1). Furthermore, a comparison of the η^{-1}-values for the August 2006 and June 2011 southern SSEs (M_w 6.0/event and M_w 5.5/event, respectively) shows that the 2011 SSE induced seismicity more efficiently than the 2006 SSE. For the northern SSE in March 2008, no significant seismicity-triggering effect was recognized, regardless of the co-SSE or post-SSE effects (Figure S3b in Supporting Information S1).

We note that the η^{-1}-values estimated in the Hikurangi Trench are roughly comparable to those in the Sagami Trough in eastern Japan (Okutani & Ide, 2011; Reverso et al., 2016). Okutani and Ide (2011) reported that the 2007 M_w 6.6 Boso-Oki SSE in the Sagami Trough triggered approximately 30 M 2.0 or larger background earthquakes based on analyses of the ETAS model. This estimate cannot be directly used because of the difference in the minimum magnitudes of the ETAS model analyses in Okutani and Ide (2011) and this study. Therefore, we used the *b*-value of Gutenberg–Richter's relationship (Aki, 1965; Gutenberg & Richter, 1944), which is approximately 0.62 for the data set of Okutani and Ide (2011), and estimated the number of M 2.5 or larger background earthquakes triggered by the 2007 Boso-Oki SSE from the number of M 2.0 or larger background earthquakes. As a result, we obtained an approximate estimate of the η^{-1}-value (= M_w 5.8 per single M 2.5 or larger event). This η^{-1}-value is smaller than that of the 2006 southern SSE in the Hikurangi Trench (M_w 6.0/event) and larger than that of the 2011 southern SSE (M_w 5.5/event). Similarly, the 2002 Boso-Oki SSE also yielded a comparable η^{-1}-value (= M_w 5.9/event). It is intriguing that the Hikurangi Trench and Sagami Trough yielded similar η^{-1}-values despite the difference in the types of SSE-induced earthquakes: interplate earthquakes in the Sagami Trough and mostly intraslab earthquakes in the Hikurangi Trench (Nishikawa et al., 2021).

The cause of the observed diversity in the seismicity-triggering effects in the Hikurangi Trench is unclear. However, we noticed that the tectonic structure substantially differed between the south-central and north-central parts of the Hikurangi Trench (Figure 1a). The south-central part (the source region of the 2006 and 2011 southern SSEs) is characterized by a well-developed accretionary wedge. In contrast, the north-central part (the source region of the 2008 northern SSEs) is undergoing tectonic erosion (Wallace, 2020). This tectonic difference might be related to the differences in the seismicity-triggering effects between the southern and northern SSEs.

The RSF seismicity model (Dieterich, 1994), a stress-based seismicity model derived from rock friction experiments (Dieterich, 1979), is often used to understand the physical mechanisms of earthquake swarm activity (e.g., Toda et al., 2002). This model has been used to explain the co-SSE seismicity-triggering effect (Segall et al., 2006). However, it is difficult to explain the substantial delay (18 days) of the increased seismicity rate with respect to the August 2006 southern SSE (Figures 5a and 5b) using the RSF seismicity model because the seismicity rate predicted is strongly controlled by the stressing rate on a fault, which correlates well with the SSE moment rate. Assuming a large value for the frictional parameter **A** (the parameter controlling the strengthening of a fault in response to an increase in sliding velocity) and effective normal stress σ in the RSF seismicity model could reproduce some delay, but the substantial delay in Figures 5a and 5b is unlikely (see the discussion in Text S4 in Supporting Information S1 for details).

In light of the above, we speculate that in addition to SSE-induced stress changes, other factors are related to the diversity in seismicity-triggering effects in the Hikurangi Trench; one of the possible factors is crustal fluids. Migrating crustal fluids can induce increases in the seismicity rate (e.g., Ross et al., 2020; Tsuneishi & Nakamura, 1970) because they reduce the frictional strength of faults (e.g., Raleigh et al., 1976). Shaddox and Schwartz (2019) and Nishikawa et al. (2021) suggested that not only co-SSE stress loading but also fluid migration following SSEs is involved in triggering the seismicity associated with SSEs in the Hikurangi Trench. Consistent with their hypothesis, a stress inversion analysis in the Hikurangi Trench (Warren-Smith et al., 2019) implied that fluid release from the subducting oceanic crust into the plate boundary and upper plate had synchronized with SSEs. Given this hypothesis, the observed diversity in seismicity-triggering effects may partly reflect differences in fluid migration following each SSE. Specifically, the seismicity rate increase 18 days after the August 2006 southern SSE (Figures 5a and 5b) may have been triggered by fluid migration

following the SSE, while such migration may have been absent or too small to detect for the June 2011 southern and March 2008 northern SSEs. Further observations and detailed analyses are required to verify this hypothesis and interpretation.

As demonstrated above, our new model is useful for quantifying the characteristics of seismicity associated with SSEs. We propose that applying our model to SSEs and seismicity in other subduction zones, such as the Sagami Trough (Ozawa et al., 2003), Nankai Trough (Yamamoto et al., 2022), Japan Trench (Nishikawa et al., 2023), and Ecuador Trench (Collot et al., 2017) is an important future direction. The post-SSE seismicity-triggering effect has not been examined for SSEs in these subduction zones. We expect that quantifying the characteristics (e.g., the η^{-1}-value and lag time τ) of seismicity associated with SSEs in subduction zones worldwide in a systematic manner using an identical model will lead to a better understanding of the relationship between SSEs and fast, regular earthquakes and better forecasts of subduction zone seismicity.

### 4.2. Influence of the Uncertainty in the SSE Moment Rates on Model Performance

In this section, we examine the influence of uncertainty in SSE moment rates on the MAP estimates of η and ΔAICs for the August 2006 and June 2011 southern SSEs, for which we observed significant seismicity rate increases associated with SSEs. As mentioned in Section 3.2.1, Wallace et al. (2012) pointed out that the June 2011 southern SSE could be divided into successive southern and northern subevents. Considering this, we also examined the influence of the two subevents on the MAP estimate of η and ΔAIC for the southern SSE in June 2011.

We estimated moment rate uncertainty using bootstrap resampling (Efron & Tibshirani, 1994; Okuda & Ide, 2018). We randomly resampled the same number of GNSS stations as used in our analysis in Section 3, allowing for duplication. We obtained 1,000 bootstrap samples and estimated the SSE moment rate for each sample. Figure 12 shows the 95% bootstrap confidence intervals for the moment rates of the southern SSEs in August 2006 and June 2011.

From the 1,000 bootstrap samples, we selected four extreme-type moment-rate functions that fell approximately within the 95% bootstrap confidence interval. For the August 2006 southern SSE, we selected moment-rate functions with a large moment, small moment, large peak moment rate, and small peak moment rate (Figure 12a). For the June 2011 southern SSE, we selected moment-rate functions with a large moment and large peak moment rate, a small moment and small peak moment rate, an earlier moment-rate peak, and a later moment-rate peak (Figure 12b). The difference between the dates of the earlier and later peaks was approximately 12 d. This large variation in the moment-rate peak date is probably because the June 2011 southern SSE can be divided into successive southern and northern subevents (Wallace et al., 2012); the dates of the earlier and later peaks are similar to those estimated for the two subsets of GNSS stations corresponding to the northern and southern subevents (GNSS stations south and north of 40.6°S, respectively) (see Figures S4–S6 in Supporting Information S1).

We estimated η-values and computed ΔAICs for these extreme-type moment-rate functions and evaluated the influence of the differences in the moment rates on the η-values and ΔAICs. The η^{-1} and ΔAIC values obtained are listed in Tables S2 and S3 in Supporting Information S1. For the August 2006 southern SSE, the MAP estimates of η^{-1} ranged from M_w 5.8/event to M_w 6.0/event. Furthermore, the ΔAIC was less than −2 for all the extreme-type moment-rate functions. These results suggest that the new model is better than the original ETAS model, even when considering moment rate uncertainty.

For the June 2011 southern SSE, the MAP estimates of η^{-1} were between M_w 5.5/event and M_w 5.9/event. For the moment-rate functions with a large moment and large peak moment rate, a small moment and small peak moment rate, and an earlier moment-rate peak, ΔAIC was less than −2, indicating the superiority of the new model over the original ETAS model. However, for the moment-rate function with a later peak, the ΔAIC was −0.8, suggesting that the model improvement was not significant. We obtained a similar result when we used the moment-rate functions corresponding to the two subevents (Figure S6 in Supporting Information S1). For the earlier southern subevent, η^{-1} and ΔAIC were M_w 5.4/event and −35.0, respectively, while $\eta^{-1} = M_w$ 5.7/event and ΔAIC = −5.7 for the later northern subevent. Although both ΔAICs were smaller than −2, the decrease in ΔAIC for the later northern subevent was substantially smaller than that for the earlier southern subevent. Furthermore, η^{-1} (i.e., the SSE moment magnitude required to trigger a single M 2.5 or greater earthquake) for the later subevent was larger than that of the earlier subevent. These results consistently suggest that the later northern subevent induced earthquakes less efficiently than the earlier southern subevent did.
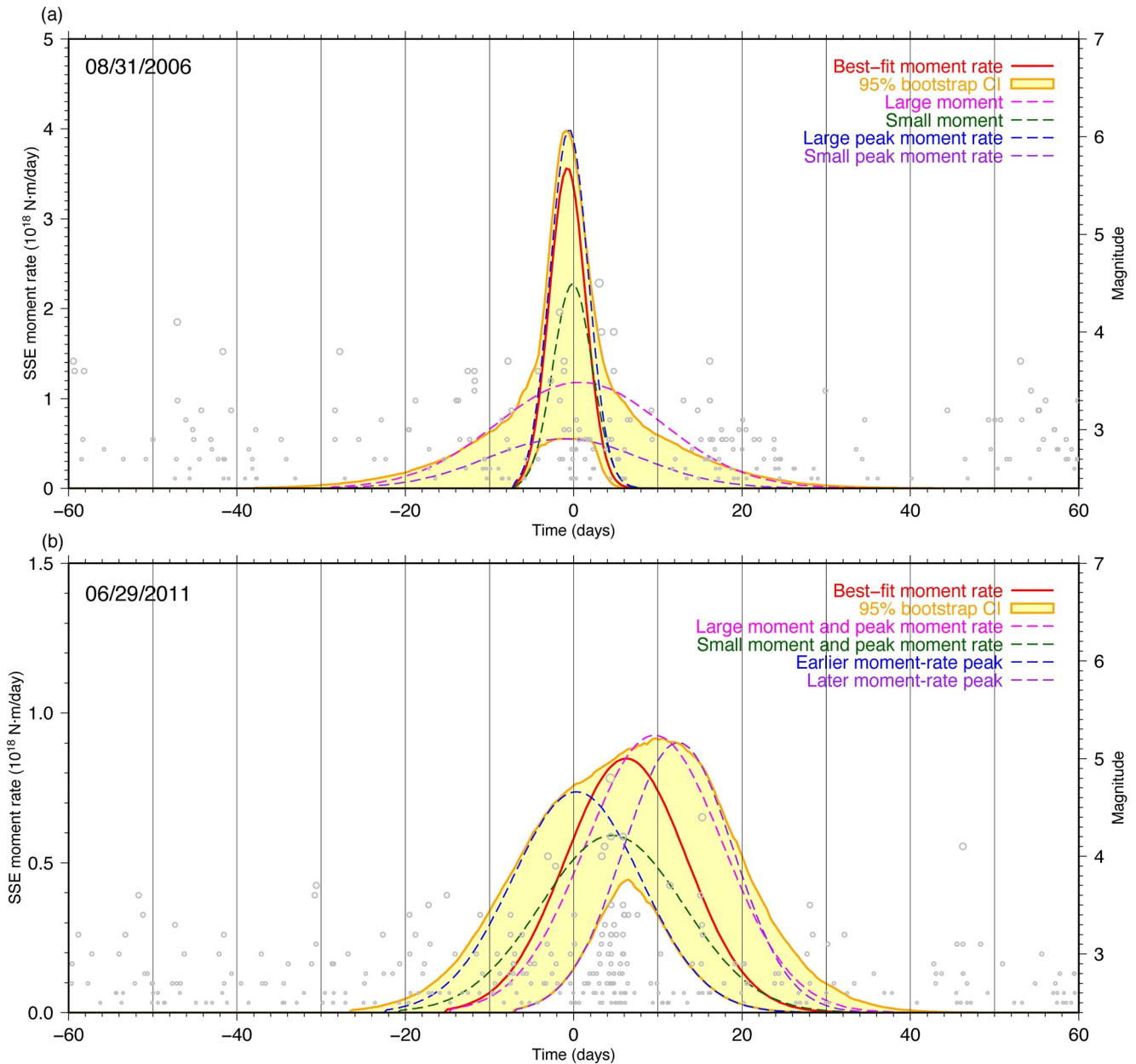
Figure 12. 95% bootstrap confidence intervals of the SSE moment rates. (a) Moment rate and its confidence interval for the August 2006 southern SSE. (b) Moment rate and its confidence interval for the June 2011 southern SSE. The solid red lines indicate the best-fit moment-rate function. Yellow areas show the 95% bootstrap confidence intervals for the moment rates. The other dashed colored lines indicate the selected extreme-type moment-rate functions. We also showed magnitude-time diagrams of earthquakes used in the ETAS analysis (gray circles) for comparison. ETAS, epidemic-type aftershock-sequence; SSE, slow slip event.

4.3. Influence of the SSEs on Aftershock Productivity

As described in Section 2.3.1, Llenos et al. (2009) found that SSEs predominantly influence background seismicity without substantially changing aftershock productivity (K). Based on these observations, in Section 3, we disregarded the influence of SSEs on aftershock productivity to simplify our model and analyses.

Although this simplification seems reasonable and has been used in several studies (e.g., Llenos et al., 2009; Llenos & McGuire, 2011; Okutani & Ide, 2011; Reverso et al., 2016), the SSEs in the Hikurangi Trench may have a detectable influence on aftershock productivity. Moreover, their influence on aftershock productivity could be a possible future way to further improve the ETAS model. In light of the above, in this section, we present our preliminary attempt to consider this influence.

For simplicity, we assume different stationary K-values during the non-SSE and SSE periods (K_0 and K_1, respectively) in Equation 2. We call this the K-variable model. Examining more complex functional forms of $K(t)$ will be the subject of future research. We applied this model to the southern SSEs of August 2006 and June 2011, for which we observed significant SSE-induced seismicity in Section 3. In the K-variable model, we use the identical p-value for the SSE and non-SSE periods. Therefore, K_0 and K_1 have the same dimension (see Section 2.3.1).

As a result, for the August 2006 southern SSE, ΔAIC increased from -6.6 to -5.0; the model did not improve by considering the influence of the SSE on aftershock productivity. The K-value during the SSE period ($K_1 = 0.91 \times 10^{-2}$) decreased to approximately 80% of that of the non-SSE period ($K_0 = 1.1 \times 10^{-2}$). The η'-value increased from 14 to 16, and the decrease in the K-value was compensated for by the increase in the η'-value. In contrast, for the June 2011 southern SSE, ΔAIC decreased from -30.4 to -36.8, indicating that the K-variable model was superior to the model with a stationary K-value. The K-value during the SSE period ($K_1 = 1.4 \times 10^{-2}$) increased to approximately twice that of the non-SSE period ($K_0 = 0.60 \times 10^{-2}$), with the η'-value decreasing from 62 to 40. Furthermore, in Figure S7 in Supporting Information S1, we found that the predictions by the K-variable model (i.e., the transformed time of the K-variable model) (yellow circles) were closer to the observed earthquake count (black solid line with a slope of unity) than those of the other models (blue and red circles). Specifically, during the period when the cumulative earthquake count was between 65 and 125 (between the two dashed magenta lines in Figure 7c and Figure S7 in Supporting Information S1), the predicted earthquake count of the K-variable model (36.9 events) was larger than that of the model with a stationary K-value (red circles) (28.2 events), although there was still a large discrepancy between the predicted and observed values (60 events).

In summary, we identified no significant change in aftershock productivity for the August 2006 southern SSE, but we did find a significant change for the June 2011 southern SSE. In the Hikurangi Trench, the influence of SSEs on aftershock productivity may vary from one SSE to another. Further detailed investigation is required to confirm this inference. We note that such variations in the influence on aftershock productivity among SSEs seem to be unexpected from the RSF seismicity model because both the background seismicity rate and the aftershock rate immediately following a mainshock increase with the stressing rate in this model (Dieterich, 1994; Llenos et al., 2009).

Lastly, we would like to comment on the relationship between aftershock productivity and SSE duration. As can be seen from Equation 2, K is a parameter that controls the aftershock rate (the number of aftershocks per unit time). Therefore, it is not directly related to the SSE duration. In our model, SSEs with different durations can have the same K-value. In this case, the SSE with a longer duration will have more aftershocks. This is simply because the interval of time integration of the aftershock occurrence rate is longer.

4.4. Power-Law Relation Between the SSE Moment Rate and Seismicity Rate

Based on the observations in the Sagami Trough of eastern Japan (Fukuda, 2018; Reverso et al., 2016), we assumed a linear relationship between the SSE moment rate and seismicity rate in most of our analyses. However, the linear relationship is not self-evident and should be verified by analyses. Therefore, this study introduced a power exponent γ (Equation 3) and examined whether the model improves by setting $\gamma \neq 1$ in Sections 3.1.3, 3.2.3, and 3.3.3. The results showed that there was no significant improvement in model performance for all the analyzed SSEs in terms of AIC. In other words, the observations of the three SSEs in the Hikurangi Trench did not suggest $\gamma \neq 1$.

This study is the first to examine the power exponent of the equation relating the SSE moment rate to the seismicity rate using a modified ETAS model. Although the previous study (Reverso et al., 2016) and this study prefer the linear relationship, the power exponent should not be concluded from the small number of observations but should be extensively examined for many more SSEs and in other subduction zones in the future. We expect that further investigations of the power exponent will provide insight into the physical mechanism of SSE-induced seismicity.

4.5. Limitations and Future Directions of This Study

This study aimed to develop the first ETAS model explicitly incorporating SSE moment rates. As a first step in improving the existing ETAS models, we worked to improve the temporal ETAS model (Ogata, 1988). However, seismicity associated with SSEs has spatiotemporal variations (e.g., epicentral migration) (Fukuda, 2018; Wallace

et al., 2012). There are also spatial variations in the magnitude of the seismicity-triggering effects of SSEs, as suggested by additional analyses in Text S1 in Supporting Information S1, in which we investigated the influence of the size of the study regions on our results. Therefore, improving the spatiotemporal ETAS model is important.

However, it is not straightforward. The spatiotemporal ETAS model is much more complex than the temporal ETAS model (Ogata, 2011; Reverso et al., 2016; Zhuang et al., 2002). There are also many challenges in improving it, such as considering the detailed spatiotemporal evolutions of SSE slips and their uncertainty and overcoming the instability of parameter estimation in the spatiotemporal ETAS model (Nishikawa & Ide, 2017). We leave overcoming these challenges for future work, as it goes far beyond the purpose of this study, which is to propose a pioneering model that explicitly incorporates the source properties of SSEs.

Here we only briefly discuss possible future directions for improving the spatiotemporal ETAS model. A direct extension of our model would be to make $A(t)$ in Equation 2 a spatiotemporal dependent $A(t, x, y)$, where x and y are spatial coordinates. In this model, $A(t, x, y)$ may depend on the stressing rate calculated from the SSE slip distribution, rather than the SSE moment rate $\dot{M}_0^{SSE}(t)$. However, because the stress loading rate depends on the details of the spatiotemporal evolution of the SSE slip, a simplified spatiotemporal evolution such as that of this study (Section 2.4) may be unsuitable, and a more sophisticated slip inversion such as that performed by Fukuda (2018) may be required.

As a more technically simple extension, $\mu + A(t)$ (i.e., the background seismicity rate) in Equation 2 could be replaced by $\mu(x, y) \cdot (1 + A(t))$, where $A(t)$ depends on the moment rate $\dot{M}_0^{SSE}(t)$ as in Equation 4. In this model, we do not need to know the detailed spatiotemporal evolution of the SSE. Instead, this model assumes that SSE-induced seismicity occurs in areas with high rates of stationary background seismicity $\mu(x, y)$. This may be a reasonable assumption because the epicenters of earthquakes during the SSE periods and outside the SSE periods generally overlap in Figures 3a and 7a.

4.6. Detection of Earthquakes Potentially Triggered by SSEs

Our new model can potentially be used to detect earthquakes induced by previously unknown SSEs. In this application, the functional form of the SSE moment rate (e.g., duration) must be assumed beforehand. As a test, we examined whether our model could detect earthquakes associated with large SSEs in the northern study region in the 2009–2011 period based solely on seismicity data. Here we used the moment rate of the August 2006 SSE in the southern study regions (13 days in duration).

We assumed that an SSE had started at time t_{SSE} and induced earthquakes and examined how much the assumption would decrease the AIC value. We varied t_{SSE} from January 2009 to December 2011 (see Figure S8 in Supporting Information S1). We extracted earthquakes that occurred during the periods when ΔAIC was −2 or smaller and considered these earthquakes as those potentially triggered by SSEs (Figure S8b in Supporting Information S1). As a result, we detected five temporal clusters (Figure S8c in Supporting Information S1).

Two large SSEs ($M_w \geq 6.7$) (January to February and March to April of 2010) are known to have occurred during the period (January 2009 to December 2011) (Wallace & Beavan, 2010). We found that one of the detected clusters (orange circles in Figure S8 in Supporting Information S1) was associated with the later SSE. However, no clusters related to the earlier SSE were found, which implies that the magnitude of the seismicity-triggering effects may vary from one SSE to another (see also Section 4.1). We note that the other four clusters are unrelated to known large SSEs. These clusters may be associated with smaller SSEs or other aseismic phenomena, such as fluid migration. Further detailed analysis is needed to identify the causes of these clusters.

5. Conclusions

We developed a new ETAS model that explicitly incorporates SSE moment rates (Section 2) and applied it to SSEs in the Hikurangi Trench (Section 3). This new model improved the forecasts of seismicity associated with SSEs in the Hikurangi Trench. Moreover, the model helped quantify the characteristics of the SSE-induced seismicity.

In the Hikurangi Trench, the characteristics of the SSE-induced background seismicity varied from one SSE to another (Section 4.1). Specifically, we observed SSEs, with and without a significant co-SSE triggering

effect. Furthermore, we observed an SSE with significant post-SSE seismicity triggering. The diversity of the seismicity-triggering effects may be related to the presence or absence of crustal fluid migration following SSEs (Nishikawa et al., 2021; Shaddox & Schwartz, 2019; Warren-Smith et al., 2019) because the above observations appear to be difficult to fully reproduce using a stress-based seismicity model (Dieterich, 1994). In addition, we observed SSEs inducing and not inducing a significant change in aftershock productivity (Section 4.3); thus, there is great diversity in the characteristics of seismicity associated with SSEs in the Hikurangi Trench. Identifying its physical mechanisms is an important direction for future research.

We propose that applying our new ETAS model to various subduction zones will lead to quantification of the characteristics of SSE-induced seismicity globally (e.g., SSE-induced background seismicity and SSE-induced changes in aftershock productivity) and reveal their regional differences. For this purpose, we need not only regional earthquake catalogs but also regional SSE catalogs in which the source properties of SSEs (e.g., spatiotemporal slip evolutions and moment-rate functions) are recorded. However, such datasets have not yet been well developed. Developing such catalogs for subduction zones worldwide is key to further advancing seismicity modeling studies.

Data Availability Statement

The GeoNet earthquake catalog is available at https://www.geonet.org.nz/data/types/eq_catalogue. Global navigation satellite system time-series data are available at https://www.geonet.org.nz/data/types/geodetic. Topography data (Smith & Sandwell, 1997) were obtained from https://topex.ucsd.edu/marine_topo/. Slab geometry (Hayes, 2018) is available at https://www.sciencebase.gov/catalog/item/5aa1b00ee4b0b1c392e86467. The plate motion and plate boundary data (Bird, 2003) were obtained from http://peterbird.name/publications/2003_PB2002/2003_PB2002.htm. Python software emcee (Foreman-Mackey et al., 2013) is available at https://emcee.readthedocs.io/en/stable/. Fortran software TDEFNODE (McCaffrey, 2009) is available at https://robmccaffrey.github.io/TDEFNODE/TDEFNODE.html. The figures were prepared using the Generic Mapping Tools software package (Wessel et al., 2019), available at https://www.generic-mapping-tools.org.

References

Akaike, H. (1974). A new look at the statistical model identification. *IEEE Transactions on Automatic Control*, *19*(6), 716–723. https://doi.org/10.1109/TAC.1974.1100705

Aki, K. (1965). Maximum likelihood estimate of b in the formula log N = a-bM and its confidence limits. *Bulletin of the Earthquake Research Institute*, *43*, 237–239.

Bird, P. (2003). An updated digital model of plate boundaries. *Geochemistry, Geophysics, Geosystems*, *4*(3), 1027. https://doi.org/10.1029/2001GC000252

Collot, J. Y., Sanclemente, E., Nocquet, J. M., Leprêtre, A., Ribodetti, A., Jarrin, P., et al. (2017). Subducted oceanic relief locks the shallow megathrust in central Ecuador. *Journal of Geophysical Research: Solid Earth*, *122*(5), 3286–3305. https://doi.org/10.1002/2016JB013849

Cruz-Atienza, V. M., Tago, J., Villafuerte, C., Wei, M., Garza-Girón, R., Dominguez, L. A., et al. (2021). Short-term interaction between silent and devastating earthquakes in Mexico. *Nature Communications*, *12*(1), 2171. https://doi.org/10.1038/s41467-021-22326-6

Delahaye, E. J., Townend, J., Reyners, M. E., & Rogers, G. (2009). Microseismicity but no tremor accompanying slow slip in the Hikurangi subduction zone, New Zealand. *Earth and Planetary Science Letters*, *277*(1–2), 21–28. https://doi.org/10.1016/j.epsl.2008.09.038

Dieterich, J. (1994). A constitutive law for rate of earthquake production and its application to earthquake clustering. *Journal of Geophysical Research*, *99*(B2), 2601–2618. https://doi.org/10.1029/93JB02581

Dieterich, J. H. (1979). Modeling of rock friction: 1. Experimental results and constitutive equations. *Journal of Geophysical Research*, *84*(B5), 2161–2168. https://doi.org/10.1029/JB084iB05p02161

Efron, B., & Tibshirani, R. J. (1994). *An introduction to the bootstrap*. CRC Press.

Foreman-Mackey, D., Hogg, D. W., Lang, D., & Goodman, J. (2013). emcee: The MCMC hammer. *Publications of the Astronomical Society of the Pacific*, *125*(925), 306–312. https://doi.org/10.1086/670067

Fukuda, J. (2018). Variability of the space-time evolution of slow slip events off the Boso Peninsula, central Japan, from 1996 to 2014. *Journal of Geophysical Research: Solid Earth*, *123*(1), 732–760. https://doi.org/10.1002/2017JB014709

Goodman, J., & Weare, J. (2010). Ensemble samplers with affine invariance. *Communications in Applied Mathematics and Computational Science*, *5*(1), 65–80. https://doi.org/10.2140/camcos.2010.5.65

Gutenberg, B., & Richter, C. F. (1944). Frequency of earthquakes in California. *Bulletin of the Seismological Society of America*, *34*(4), 185–188. https://doi.org/10.1785/BSSA0340040185

Hayes, G. (2018). *Slab2 - A comprehensive subduction zone geometry model*. U.S. Geological Survey data release. https://doi.org/10.5066/F7PV6JNV

Helmstetter, A., & Sornette, D. (2002). Subcritical and supercritical regimes in epidemic models of earthquake aftershocks. *Journal of Geophysical Research*, *107*(B10), 2237. https://doi.org/10.1029/2001JB001580

Hughes, L., Chamberlain, C. J., Townend, J., & Thomas, A. M. (2021). A repeating earthquake catalog from 2003 to 2020 for the Raukumara Peninsula, northern Hikurangi subduction margin, New Zealand. *Geochemistry, Geophysics, Geosystems*, *22*(5), e2021GC009670. https://doi.org/10.1029/2021GC009670

Ito, Y., Hino, R., Kido, M., Fujimoto, H., Osada, Y., Inazu, D., et al. (2013). Episodic slow slip events in the Japan subduction zone before the 2011 Tohoku-Oki earthquake. *Tectonophysics*, *600*, 14–26. https://doi.org/10.1016/j.tecto.2012.08.022

Jacobs, K. M., Savage, M. K., & Smith, E. C. G. (2016). Quantifying seismicity associated with slow slip events in the Hikurangi margin, New Zealand. *New Zealand Journal of Geology and Geophysics*, *59*(1), 58–69. https://doi.org/10.1080/00288306.2015.1127827

Kawasaki, I., Asai, Y., Tamura, Y., Sagiya, T., Mikami, N., Okada, Y., et al. (1995). The 1992 Sanriku-oki, Japan, ultra-slow earthquake. *Journal of Physics of the Earth*, *43*(2), 105–116. https://doi.org/10.4294/jpe1952.43.105

Liu, Y., Rice, J. R., & Larson, K. M. (2007). Seismicity variations associated with aseismic transients in Guerrero, Mexico, 1995–2006. *Earth and Planetary Science Letters*, *262*(3–4), 493–504. https://doi.org/10.1016/j.epsl.2007.08.018

Llenos, A. L., & McGuire, J. J. (2011). Detecting aseismic strain transients from seismicity data. *Journal of Geophysical Research*, *116*(B6), B06305. https://doi.org/10.1029/2010JB007537

Llenos, A. L., McGuire, J. J., & Ogata, Y. (2009). Modeling seismic swarms triggered by aseismic transients. *Earth and Planetary Science Letters*, *281*(1–2), 59–69. https://doi.org/10.1016/j.epsl.2009.02.011

Llenos, A. L., & Michael, A. J. (2019). Ensembles of ETAS models provide optimal operational earthquake forecasting during swarms: Insights from the 2015 San Ramon, California swarm. *Bulletin of the Seismological Society of America*, *109*(6), 2145–2158. https://doi.org/10.1785/0120190020

Marsan, D., Reverso, T., Helmstetter, A., & Enescu, B. (2013). Slow slip and aseismic deformation episodes associated with the subducting Pacific plate offshore Japan, revealed by changes in seismicity. *Journal of Geophysical Research: Solid Earth*, *118*(9), 4900–4909. https://doi.org/10.1002/jgrb.50323

McCaffrey, R. (2009). Time-dependent inversion of three-component continuous GPS for steady and transient sources in northern Cascadia. *Geophysical Research Letters*, *36*(7), L07304. https://doi.org/10.1029/2008GL036784

Nelder, J. A., & Mead, R. (1965). A simplex method for function minimization. *The Computer Journal*, *7*(4), 308–313. https://doi.org/10.1093/comjnl/7.4.308

Nishikawa, T., & Ide, S. (2017). Detection of earthquake swarms at subduction zones globally: Insights into tectonic controls on swarm activity. *Journal of Geophysical Research: Solid Earth*, *122*(7), 5325–5343. https://doi.org/10.1002/2017JB014188

Nishikawa, T., & Ide, S. (2018). Recurring slow slip events and earthquake nucleation in the source region of the M 7 Ibaraki-Oki earthquakes revealed by earthquake swarm and foreshock activity. *Journal of Geophysical Research: Solid Earth*, *123*(9), 7950–7968. https://doi.org/10.1029/2018JB015642

Nishikawa, T., Ide, S., & Nishimura, T. (2023). A review on slow earthquakes in the Japan Trench. *Progress in Earth and Planetary Science*, *10*, 1. https://doi.org/10.1186/s40645-022-00528-w

Nishikawa, T., Nishimura, T., & Okada, Y. (2021). Earthquake swarm detection along the Hikurangi Trench, New Zealand: Insights into the relationship between seismicity and slow slip events. *Journal of Geophysical Research: Solid Earth*, *126*(4), e2020JB020618. https://doi.org/10.1029/2020JB020618

Ogata, Y. (1988). Statistical models for earthquake occurrences and residual analysis for point processes. *Journal of the American Statistical Association*, *83*(401), 9–27. https://doi.org/10.1080/01621459.1988.10478560

Ogata, Y. (2011). Significant improvements of the space-time ETAS model for forecasting of accurate baseline seismicity. *Earth Planets and Space*, *63*(3), 217–229. https://doi.org/10.5047/eps.2010.09.001

Okada, Y., Nishimura, T., Tabei, T., Matsushima, T., & Hirose, H. (2022). Development of a detection method for short-term slow slip events using GNSS data and its application to the Nankai subduction zone. *Earth Planets and Space*, *74*(1), 18. https://doi.org/10.1186/s40623-022-01576-8

Okuda, T., & Ide, S. (2018). Streak and hierarchical structures of the Tohoku–Hokkaido subduction zone plate boundary. *Earth Planets and Space*, *70*(1), 132. https://doi.org/10.1186/s40623-018-0903-8

Okutani, T., & Ide, S. (2011). Statistic analysis of swarm activities around the Boso Peninsula, Japan: Slow slip events beneath Tokyo Bay? *Earth Planets and Space*, *63*(5), 419–426. https://doi.org/10.5047/eps.2011.02.010

Omi, T., Ogata, Y., Hirata, Y., & Aihara, K. (2015). Intermediate-term forecasting of aftershocks from an early aftershock sequence: Bayesian and ensemble forecasting approaches. *Journal of Geophysical Research: Solid Earth*, *120*(4), 2561–2578. https://doi.org/10.1002/2014JB011456

Ozawa, S., Miyazaki, S., Hatanaka, Y., Imakiire, T., Kaidzu, M., & Murakami, M. (2003). Characteristic silent earthquakes in the eastern part of the Boso peninsula, Central Japan. *Geophysical Research Letters*, *30*(6), 1238. https://doi.org/10.1029/2002GL016665

Radiguet, M., Perfettini, H., Cotte, N., Gualandi, A., Valette, B., Kostoglodov, V., et al. (2016). Triggering of the 2014 Mw 7.3 Papanoa earthquake by a slow slip event in Guerrero, Mexico. *Nature Geoscience*, *9*(11), 829–833. https://doi.org/10.1038/ngeo2817

Raleigh, C. B., Healy, J. H., & Bredehoeft, J. D. (1976). An experiment in earthquake control at Rangely, Colorado. *Science*, *191*(4233), 1230–1237. https://doi.org/10.1126/science.191.4233.1230

Reverso, T., Marsan, D., Helmstetter, A., & Enescu, B. (2016). Background seismicity in Boso Peninsula, Japan: Long-term acceleration, and relationship with slow slip events. *Geophysical Research Letters*, *43*(11), 5671–5679. https://doi.org/10.1002/2016GL068524

Ross, Z. E., Cochran, E. S., Trugman, D. T., & Smith, J. D. (2020). 3D fault architecture controls the dynamism of earthquake swarms. *Science*, *368*(6497), 1357–1361. https://doi.org/10.1126/science.abb077

Schorlemmer, D., Werner, M. J., Marzocchi, W., Jordan, T. H., Ogata, Y., Jackson, D. D., et al. (2018). The collaboratory for the study of earthquake predictability: Achievements and priorities. *Seismological Research Letters*, *89*(4), 1305–1313. https://doi.org/10.1785/0220180053

Segall, P., Desmarais, E. K., Shelly, D., Miklius, A., & Cervelli, P. (2006). Earthquakes triggered by silent slip events on Kīlauea volcano, Hawaii. *Nature*, *442*(7098), 71–74. https://doi.org/10.1038/nature04938

Shaddox, H. R., & Schwartz, S. Y. (2019). Subducted seamount diverts shallow slow slip to the forearc of the northern Hikurangi subduction zone, New Zealand. *Geology*, *47*(5), 415–418. https://doi.org/10.1130/G45810.1

Smith, W. H., & Sandwell, D. T. (1997). Global sea floor topography from satellite altimetry and ship depth soundings. *Science*, *277*(5334), 1956–1962. https://doi.org/10.1126/science.277.5334.1956

Socquet, A., Valdes, J. P., Jara, J., Cotton, F., Walpersdorf, A., Cotte, N., et al. (2017). An 8 month slow slip event triggers progressive nucleation of the 2014 Chile megathrust. *Geophysical Research Letters*, *44*(9), 4046–4053. https://doi.org/10.1002/2017GL073023

Toda, S., Stein, R. S., & Sagiya, T. (2002). Evidence from the AD 2000 Izu islands earthquake swarm that stressing rate governs seismicity. *Nature*, *419*(6902), 58–61. https://doi.org/10.1038/nature00997

Todd, E. K., Schwartz, S. Y., Mochizuki, K., Wallace, L. M., Sheehan, A. F., Webb, S. C., et al. (2018). Earthquakes and tremor linked to seamount subduction during shallow slow slip at the Hikurangi margin, New Zealand. *Journal of Geophysical Research: Solid Earth*, *123*(8), 6769–6783. https://doi.org/10.1029/2018JB016136

Tsuneishi, Y., & Nakamura, K. (1970). Faulting associated with the Matsushiro swarm earthquakes. *Bulletin of the Earthquake Research Institute*, *48*, 29–51.

Utsu, T. (1957). Magnitudes of earthquakes and occurrence of their aftershocks (in Japanese with English figure captions). *Zisin (Journal of the Seismological Society of Japan) Series*, *2 10*(1), 35–45. https://doi.org/10.4294/zisin1948.10.1_35

Utsu, T., Ogata, Y., Matsu'ura, R., & Matsu'ura (1995). The centenary of the Omori formula for a decay law of aftershock activity. *Journal of Physics of the Earth*, *43*(1), 1–33. https://doi.org/10.4294/jpe1952.43.1

Vallée, M., Nocquet, J. M., Battaglia, J., Font, Y., Segovia, M., Regnier, M., et al. (2013). Intense interface seismicity triggered by a shallow slow slip event in the Central Ecuador subduction zone. *Journal of Geophysical Research: Solid Earth*, *118*(6), 2965–2981. https://doi.org/10.1002/jgrb.50216

Villegas-Lanza, J. C., Nocquet, J. M., Rolandone, F., Vallée, M., Tavera, H., Bondoux, F., et al. (2016). A mixed seismic–aseismic stress release episode in the Andean subduction zone. *Nature Geoscience*, *9*(2), 150–154. https://doi.org/10.1038/ngeo2620

Wallace, L. M. (2020). Slow slip events in New Zealand. *Annual Review of Earth and Planetary Sciences*, *48*(1), 175–203. https://doi.org/10.1146/annurev-earth-071719-055104

Wallace, L. M., & Beavan, J. (2010). Diverse slow slip behavior at the Hikurangi subduction margin, New Zealand. *Journal of Geophysical Research*, *115*(B12), B12402. https://doi.org/10.1029/2010JB007717

Wallace, L. M., Beavan, J., Bannister, S., & Williams, C. (2012). Simultaneous long-term and short-term slow slip events at the Hikurangi subduction margin, New Zealand: Implications for processes that control slow slip event occurrence, duration, and migration. *Journal of Geophysical Research*, *117*(B11), B11402. https://doi.org/10.1029/2012JB009489

Warren-Smith, E., Fry, B., Wallace, L., Chon, E., Henrys, S., Sheehan, A., et al. (2019). Episodic stress and fluid pressure cycling in subducting oceanic crust during slow slip. *Nature Geoscience*, *12*(6), 475–481. https://doi.org/10.1038/s41561-019-0367-x

Wessel, P., Luis, J. F., Uieda, L., Scharroo, R., Wobbe, F., Smith, W. H., & Tian, D. (2019). The generic mapping tools version 6. *Geochemistry, Geophysics, Geosystems*, *20*(11), 5556–5564. https://doi.org/10.1029/2019GC008515

Wiemer, S., & Wyss, M. (2000). Minimum magnitude of completeness in earthquake catalogs: Examples from Alaska, the Western United States, and Japan. *Bulletin of the Seismological Society of America*, *90*(4), 859–869. https://doi.org/10.1785/0119990114

Woessner, J., & Wiemer, S. (2005). Assessing the quality of earthquake catalogues: Estimating the magnitude of completeness and its uncertainty. *Bulletin of the Seismological Society of America*, *95*(2), 684–8698. https://doi.org/10.1785/0120040007

Yamamoto, Y., Yada, S., Ariyoshi, K., Hori, T., & Takahashi, N. (2022). Seismicity distribution in the Tonankai and Nankai seismogenic zones and its spatiotemporal relationship with interplate coupling and slow earthquakes. *Progress in Earth and Planetary Science*, *9*(1), 32. https://doi.org/10.1186/s40645-022-00493-4

Yarce, J., Sheehan, A. F., Nakai, J. S., Schwartz, S. Y., Mochizuki, K., Savage, M. K., et al. (2019). Seismicity at the northern Hikurangi Margin, New Zealand, and investigation of the potential spatial and temporal relationships with a shallow slow slip event. *Journal of Geophysical Research: Solid Earth*, *124*(5), 4751–4766. https://doi.org/10.1029/2018JB017211

Zhuang, J., Ogata, Y., & Vere-Jones, D. (2002). Stochastic declustering of space-time earthquake occurrences. *Journal of the American Statistical Association*, *97*(458), 369–380. https://doi.org/10.1198/016214502760046925